DEVELOPMENT OF A MODEL FOR ^{11}C PRODUCTION VIA THE ^{14}N(p,α) REACTION USING A GE PETTRACE CYCLOTRON

THESIS

Amy C. Hall, Captain, USAF

AFIT-ENP-MS-19-M-080

DEPARTMENT OF THE AIR FORCE
AIR UNIVERSITY

AIR FORCE INSTITUTE OF TECHNOLOGY

Wright-Patterson Air Force Base, Ohio

DEVELOPMENT OF A MODEL FOR ^{11}C PRODUCTION VIA THE ^{14}N(p,α) REACTION USING A GE PETTRACE CYCLOTRON

THESIS

Presented to the Faculty

Department of Physics

Graduate School of Engineering and Management

Air Force Institute of Technology

Air University

Air Education and Training Command

In Partial Fulfillment of the Requirements for the

Degree of Master of Science in Nuclear Engineering

Amy C. Hall, BS

Captain, USAF

March 2019

DISTRIBUTION STATEMENT A.
APPROVED FOR PUBLIC RELEASE; DISTRIBUTION UNLIMITED.

AFIT-ENP-MS-19-M-080

DEVELOPMENT OF A MODEL FOR ^{11}C PRODUCTION VIA THE ^{14}N(p,α) REACTION USING A GE PETTRACE CYCLOTRON

Amy C. Hall, BS

Captain, USAF

Committee Membership:

Capt. J. E. Bevins
Chair

Dr. A. A. Bickley
Member

Dr. R. Ferrieri
Member

Dr. J. W. McClory
Member

AFIT-ENP-MS-19-M-080

Abstract

The GE PETtrace 800 Series cyclotron at the Missouri University Research Reactor (MURR) facility is used extensively for medical and research radioisotope production. However, no model exists of its radioisotope production performance, and the energy, full intensity, and spatial profile of the cyclotron proton beam has never been measured. To improve production planning for research and medical isotopes, a MCNP6 model of the isotope production process was developed to maximize efficiency in target design and better understand irradiation conditions. Since the cyclotron beam energy and profile has a significant impact on the types of reactions that take place and the efficiency of radioisotope production, the MURR cyclotron proton beam energy was measured via activation of a high-purity copper foil stack. Phosphor plate imaging was used to radiographically image the foil stacks in order to characterize the beam's spatial and intensity profile. The measured beam characteristics were used to define the source for a MCNP6 model of the production of ^{11}C, an important research radioisotope used for medical and plant research. The model was compared to experimental ^{11}C production data obtained using ion chamber measurements of ^{11}C production cycles at varying beam currents. Finally, the ^{11}C production target model was used to analyze inefficiencies present in the current design and operating characteristics.

To My Husband, Mom, Dad, and Sister

Acknowledgments

I would like to express my sincerest appreciation to my thesis advisor, Captain Bevins. This effort would not have been possible without his guidance and support. I would, also, like to sincerely thank my committee, Dr. Bickley, Dr. Ferrieri, and Dr. McClory for their expertise and support throughout the course this research. Finally, I would like to thank Dr. Brockman, Dr. Schueller and Dr. Wilder for their technical expertise and assistance during my experimental work and analysis.

Amy C. Hall

Table of Contents

List of Figures

List of Tables

DEVELOPMENT OF A MODEL FOR ^{11}C PRODUCTION VIA THE ^{14}N(p,α) REACTION USING A GE PETTRACE CYCLOTRON

I. Introduction

1.1 Motivation

The production of radioisotopes is extremely important for a wide variety of applications. Radioisotopes are used within the medical field to treat diseases such as cancer and hyperthyroidism and provide a means for tracking Alzheimer's, tumors, and bone injuries using positron emission tomography (PET) scans and other nuclear imaging technology [1]. Radioisotopes are also used extensively in research applications. For example, plant scientists use radioisotope tracers to track plant nutrient activity [2], and medical scientists use radio-tracers with animals to analyze disease progression and research treatment options [3]. Many radioisotopes have been used for decades, and their production is generally well established. However, radioisotope production can be costly, and as new radioisotopes are implemented for medical and research purposes, it is important to ensure that their production is efficient.

At the Missouri University Research Reactor (MURR), radioisotopes are produced daily for distribution to local hospitals and used on location to perform research studies. MURR employs the PETtrace800 series cyclotron as one of its radioisotope production tools. The cyclotron is used to produce ^{18}F ($t_{1/2}$ = 109.8 min) from the ^{18}O(p,n) reaction. ^{18}F is used in fluorodeoxyglucose, a tracer for positron emission tomography (PET) scans. PET scans are used for a wide variety of diagnostic imaging procedures to include cancer diagnosis and treatment [4].

MURR also uses radioisotopes produced by their cyclotron for important research applications related to biochemistry, nuclear engineering, and agriculture. Nuclear imaging can be used in plant bodies to provide information about the internal chemical interactions in a manner similar to the use of radio-tracers in humans. At MURR, a growing research area utilizing radioisotopes is sustainable cropping. The estimated population of the world in the year 2050 is around 9.1 billion people. Based on this estimate, it is projected that food production must become roughly 50% more efficient [5]. Nuclear imaging can be

used to gain a better understanding of plant behavior allowing for improvements in crop environments and crop yield to support a growing world population [5]. Optimizing the production of important research isotopes through a better understanding of the processes involved will allow the sustainable agriculture research to progress.

1.2 Background

John H. Lawrence is widely considered the "father of nuclear medicine." Lawrence's research focused on the production of artificial radioactive isotopes, which he believed could be used widely in medicine. John Lawrence did the majority of his radioisotope research at his brother Ernest's laboratory [6]. Many of the currently most widely used medical isotopes were discovered by Lawrence while working at the laboratory. Lawrence performed the first radiation therapy treatment on a patient with leukemia using a phosphorous-32 source in 1936 [7]. In addition to cancer treatment, early nuclear medicine capabilities were also used to treat decompression sickness for fighter pilots in World War II. After World War II, researchers began looking into using medical isotopes as tracers for medical imaging [6].

Large-scale medical isotopes are primarily produced in nuclear reactors in only a few countries including the United States, Canada, Australia, and South Africa [8]. However, radioisotopes with short half-lives must be produced on location, or at least very close to where they will be used. Such isotopes are generally produced in small batches with cyclotrons such as the MURR's PETtrace800 series cyclotron [4]. The PETtrace cyclotron is specifically designed for the production of radioactive PET tracers. In addition to radioisotope production for medical purposes, MURR also utilizes the cyclotron to produce research radioisotopes, such as ^{11}C and ^{13}N [4]. The reaction ^{14}N$(p, \alpha)^{11}$C is used to produce ^{11}C at MURR and ^{14}N$(p, pn)^{13}$N is used to produce ^{13}N. The targets that MURR uses for radioisotope production are standard General Electric (GE$^{®}$) targets that are made from aluminum with stainless steel fixtures and contain gas fill of the desired target nucleus [4].

The short-lived nature of radio-tracer isotopes is one of their most important characteristics. Tracer isotopes decay rapidly by emitting gamma rays which can be tracked

with radiation detectors. The tracer isotopes are placed within human, animal, or plant bodies in such a way that they will be transported and accumulate in regions of interest based on the desired treatment or research effort.

^{11}C is also used in biomedical research including PET research with adult female baboons. For this research ^{11}C was in the form of ^{11}C-reclopride, a dopamine-specific radio-tracer that binds to dopamine in the brain, allowing for the dopamine to be tracked in vivo (inside a living organism). ^{11}C-raclopride imaging was used to study Huntington's disease, which degrades dopamine receptors within the brain [3].

The plant science group at MURR regularly produces radioisotopes for plant studies and other chemical and biological research. A key area of interest for the plant science group is nitrogen fixation in plants which is involved in plant metabolism [9]. Plants metabolize extremely quickly and are able to uptake nutrients and minerals, including the nitrogen, within minutes of introduction. During the nitrogen fixation process, bacteria within the root system of plants produce nitrogen compounds. This process benefits the plants by helping them grow more quickly, an important consideration in improving the efficiency of food production [9].

Another area of research at MURR is the behavior of plants under duress due to herbivory. Herbivory refers to the attack and damage of plants by insects and other herbivores. When plants are attacked, they react in a variety of chemical and physiological ways to defend themselves and protect the resources they possess. For example, they have the ability to allocate chemicals within their stems and leaves to their roots to prevent them from being lost. Radio-tracer isotopes such as ^{11}C and ^{13}N can be used to observe this behavior through the use of radiation detectors [2].

In order to better understand and operate the cyclotron to enable research in these areas, characterization of the proton beam and production is desired. This research develops an experimentally informed model to characterize the ^{11}C production and explore improvements in radioisotope production efficiency.

1.3 Problem Statement

Radioisotope production is costly, so efficiency is often a significant concern. Radiation transport simulations are one method that can be used to study the efficiency of production targets. While simulations provide many advantages such as increasing the pace of research, lowering the cost, and studying difficult to measure phenomena, it can be difficult to capture all of the physics and geometry considerations for complex production environments. For example, the MURR cyclotron proton beam has not been characterized in terms of profile and energy, and the radiation transport does not capture the heat transfer dynamics that affect gas target density profiles.

The primary objective for this research is to develop an experimentally-informed model of ^{11}C production using the MURR cyclotron to enable the improvement of radioisotope production efficiency. This overall goal was sub-divided into the following objectives and sub-objectives:

1. Characterize the proton beam
   a. Measure the precise beam energy
   b. Characterize the beam profile and intensity
2. Perform ion chamber measurements and analysis of ^{11}C production to quantify ^{11}C production as a function of beam current
3. Develop a ^{11}C production simulation in Monte Carlo Neutral Particle 6.1 (MCNP6) [10]
   a. Incorporate an accurate proton beam
   b. Benchmark model against experimental measurements
   c. Assess the performance of available nuclear data libraries
4. Characterize ^{11}C production target inefficiencies

1.4 Methodology

The MURR cyclotron beam energy was characterized using isotopically natural copper foils placed directly behind the cyclotron proton beam window. The proton reactions within the copper foils produced ^{62}Zn and ^{65}Zn via the ^{63}Cu(p,2n) and ^{65}Cu(p,n) reactions, respectively. The activities of each isotope were characterized using gamma

spectroscopy. The beam energy was determined from the relative measured activity profile of each Zn isotope for each activated foil and an MCNP6 simulation of the foil activation experiment. To obtain the energy of the proton beam, the foil experimental results were compared to the simulation results at varying proton beam energy levels using Chi-squared minimization.

Additionally, the irradiated foils were radiographically imaged in order to characterize the beam spatial and intensity profile. The beam profile was characterized based on the size of the image on the first foil in the stack and the stated resolution of the film, which was cross validated using the aperture visible in the last film in the foil stack. The beam intensity was measured in a histogram format based on a pixel mesh to characterize the intensity with respect to location. The results were implemented in the MCNP6 ^{11}C simulation.

The MURR cyclotron ^{11}C production was modeled using MCNP6. The production simulation included the measured cyclotron proton beam source, the GE ^{11}C production target, and the pressurized helium filled cooling window encapsulated by Havar® foils. Additionally, the model was used to compare the two source definitions (mono-directional 16.5 MeV protons vs. the experimentally measured profile and energy). In order to benchmark the ^{11}C target simulation, an ion chamber was used to measure the amount of ^{11}C produced at varying proton beam currents.

Finally, the MCNP6 ^{11}C production model was further analyzed using a mesh tally within the target region. The mesh tally was used to characterize the production within the target and identify apparent inefficiencies in the design of the target.

1.5 Assumptions and Limitations

One limitation associated with this research is the nuclear data required to model the ^{11}C production target. The reactions of interest for these simulations cannot be effectively modeled in MCNP6 without introducing additional nuclear data not contained in the standard libraries. For example, the ^{11}C production simulation requires the specific $^{14}N(p,\alpha)^{11}C$ reaction to be modeled and tallied, but the standard MCNP6 cross-section libraries will tally all $^{14}N(p,x\alpha)^{11}C$ reactions. For this research, data was pulled from the

TALYS-based Evaluated Nuclear Data Library (TENDL) [11], the Japanese Evaluated Nuclear Data Library (JENDL) [12], the Proton Activation Data File (PADF) [13], and the Evaluated Nuclear Data File (ENDF) [14]. These additional data libraries did not always follow consistent formatting and details, such as units, and are not always particularly well documented. The choice of which libraries to include was informed by how well the evaluated data matched the measured cross-section data from the literature, and experimental data was included as well if the evaluations were found to differ significantly.

Another limitation with the ^{11}C production model is uncertainty in the beam characteristics during the irradiation runs. Specifically, the PETtrace 800 Series cyclotron has relatively large timing and beam current uncertainties. The cyclotron is designed to run with a specific beam current, irradiation time, and target. However, there is roughly a $\pm 1\,\mu A$ uncertainty in the beam current and a $\pm 30\,s$ time uncertainty at the start and stop of irradiation as the cyclotron tunes up and tunes down.

The cyclotron target design results in additional uncertainty. Production efficiency within the target likely is diminished due to the beam within the target interacting with target walls and a target that sags at the cyclotron beam port location. As the proton beam travels through the target it spreads out and likely interacts with the sides and the end of the target. As a result, less ^{11}C will be produced than would be expected based upon the cyclotron input characteristics. While characterizing the beam profile will help capture some of this behavior, no direct measurement was made to experimentally characterize these effects.

As the cyclotron beam current increases, the gas is heated resulting in gas density reduction. This effect was characterized indirectly, but due to the high uncertainty in the beam current, no experimental run was performed where the effect was thought to be negligible. The gas density reduction impacts the behavior of the gas within the target and consequently the ^{11}C production. This phenomenon is very difficult to model within MCNP6 since it would require coupled radiation and multiphysics simulation. The pressure gauge that characterizes the pressure of the target under irradiation was not working during the experimental run, further limiting the ability to incorporate the gas density reduction

effects in the model. Due to these facts, incorporation of gas density reduction effects was not accomplished in this research.

Finally, an additional limitation with the foil activation experiment was that only one high-purity germanium detector was used to measure the activated foils. If additional detectors were available and could be used to count foils simultaneously, a stack of all 25 µm foils could have been used. This would have allowed for finer resolution in the beam characterization measurements and limited the number and types of correction factors that needed to be applied in the analysis. An MCNP6 model was used to determine the best placement of each thickness of foil in order to attempt to overcome this limitation.

II. Literature Review

Radioisotopes can be used for a wide-range of purposes including medical applications and research [8]. This research concerns the production of radioisotopes that are intended to be used in medical and plant research, primarily as PET tracers. The PET tracer research performed with ^{11}C and ^{13}N at MURR can be used for developing sustainable agriculture and mental health treatments. Sustainable agriculture research attempts to improve plant performance and hardiness in order to allow for more food production and decreased risk [5]. The production of radioisotopes at MURR and some of the important applications are discussed in Section 2.1.

This research required an understanding of nuclear reactions and how to implement the evaluated nuclear data into the MCNP6 models. Each of the MCNP6 simulations used in this research necessitated the use of alternate nuclear cross-section data, which allowed for specific reactions of interest to be defined. Available cross-section evaluations were considered, and the best options were chosen based on how well they represented the data [15]. An overview of the nuclear reactions and data relevant to this research is explored in Sections 2.2 and 2.3.

In order to measure the precise cyclotron energy of the MURR cyclotron beam, previous foil activation experiments were researched [16-18]. These previous experiments, described in Section 2.4 and 2.5, were used as a baseline to design the experiments performed in this research.

The radiography and ion chamber tools used to perform the beam characterization and ^{11}C production measurements, respectively, are described in Sections 2.6 and 2.7. The ion chamber was also used to explore gas density reduction, a major factor with gaseous target radioisotope production. Gas density reduction can occur when the cyclotron beam heats the target gas and the heat is not dissipated properly which, in turn, results in inefficient radioisotope production [19]. This process is described in Section 2.8.

2.1 MURR Radioisotope Production

At MURR and other small facilities, radioisotopes are produced using specialized cyclotrons that accelerate particles to high energies to elicit nuclear reactions with target nuclei [4]. MURR employs a PETtrace800 series cyclotron specifically designed to produce radioisotopes utilized as tracers [4]. They produce ^{18}F ($t_{1/2}$ = 109.8 min) from the reaction $^{18}O(p,n)$ every night to make the medical isotope fluorodeoxyglucose, a tracer used for PET scans [4].

The target used for ^{11}C and ^{13}N production is a standard GE® radioisotope production target, depicted in Figure 1, made of aluminum with stainless steel fixtures (See target schematics in Appendix B). For ^{11}C, the target is filled with ^{14}N gas; for ^{13}N production, CO_2 fill gas is used. After irradiation, the gas is pumped out of the cyclotron target and through tubes under the floor. The gas is pulled into an ion chamber containing a carbon trap where it is analyzed to determine the amount of radioisotope produced.

Figure 1: MURR GE® standard cyclotron radioisotope production target.

In addition to the internal gas region where the target gas is pumped in and the radioisotope rich gas is pumped out, there are also ports for helium and water to cool the target during the production process. Figure 2 shows the internal components of the target. The center interior cylinder is the gas region where the target gas is filled and irradiated. The 6 other tubes shown are where water is pumped through the target for cooling.
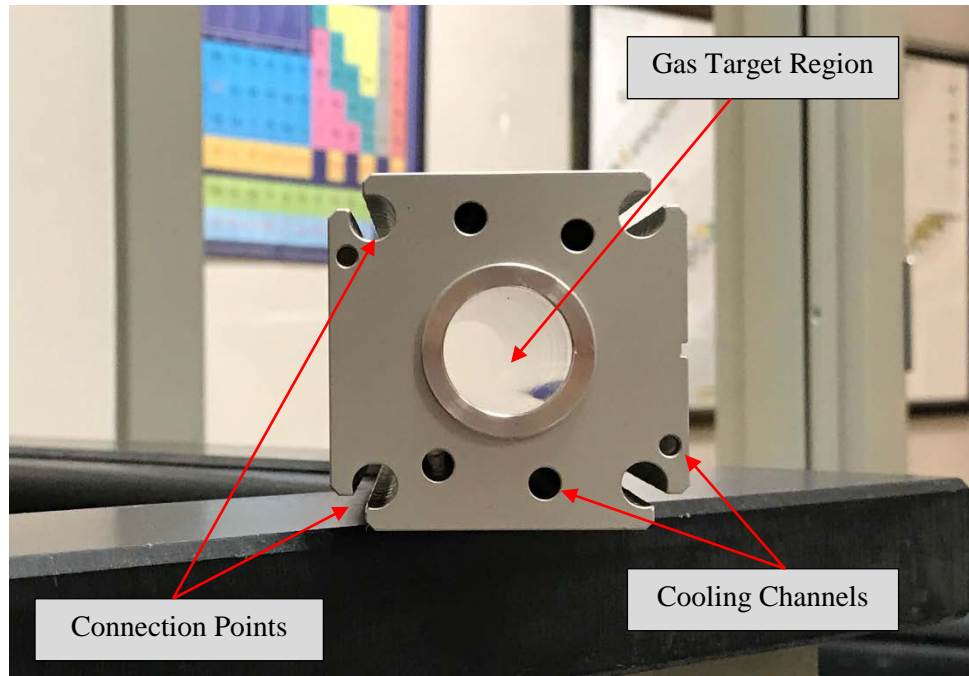
Figure 2: Internal view of the disassembled cyclotron ^{13}N and ^{11}C production target.

Helium is used for cooling a Havar® foil region located at the opposite end of the target from where the gas and water enter, i.e. the left side of the target shown in Figure 1. Figure 3 shows the ^{11}C production target including the Havar® foil window layout. The Havar® foil region separates the cyclotron vacuum at the end of the target where the proton beam enters and the pressurized fill gas region.

The PETtrace cyclotron at MURR has six ports that connect to the cyclotron allowing irradiation of up to six targets simultaneously and decreasing the costs associated with radioisotope production. Figure 4 shows the MURR PETtrace cyclotron and the six port locations. The ^{11}C target location is labeled in the image.
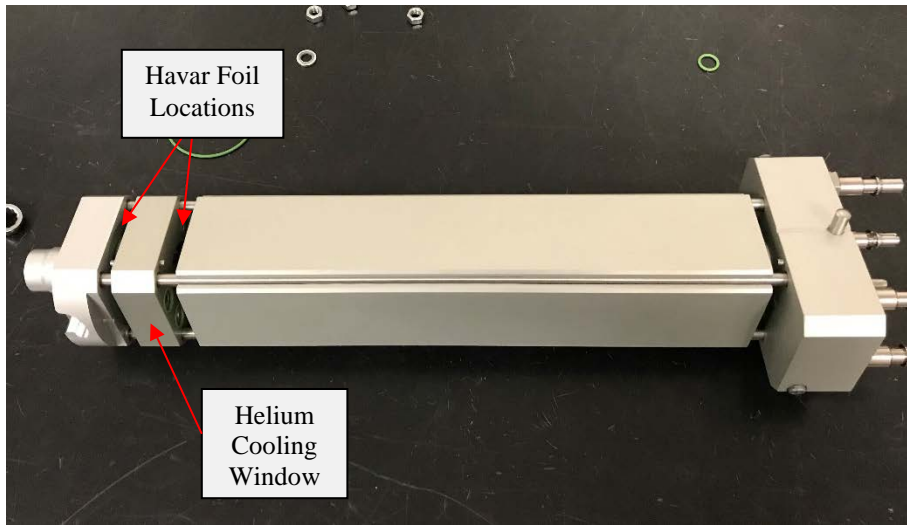
Figure 3: ^{11}C production target Havar® foil window.
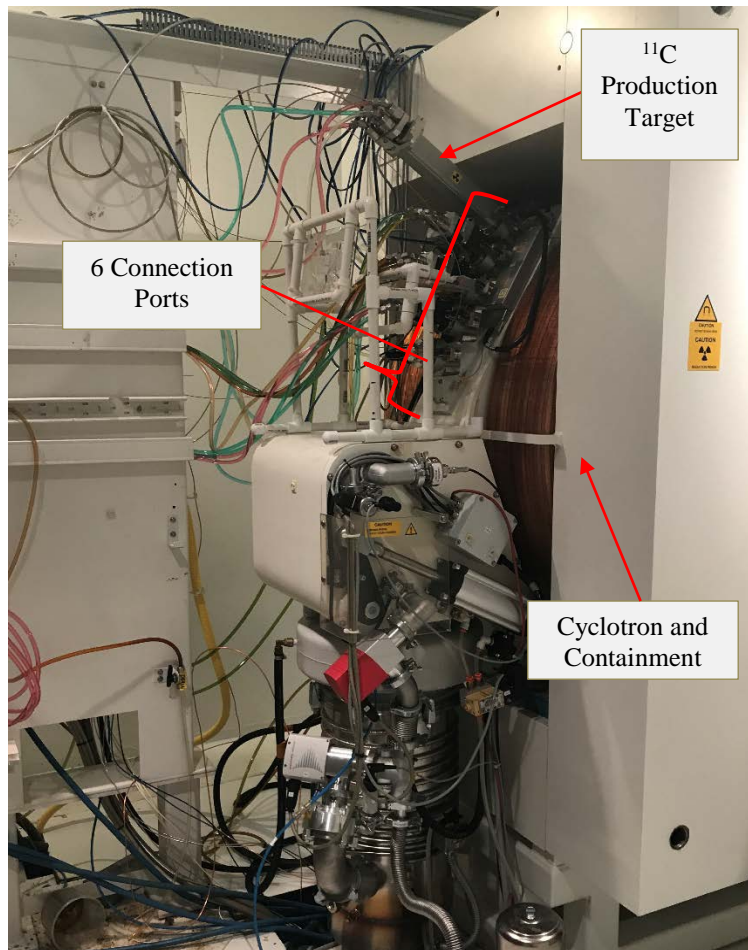
Figure 4: MURR PETtrace 800 Series cyclotron showing six ports and the ^{11}C target marked in the uppermost position.

2.1.1 Plant Science Research and Sustainable Cropping

Radioisotope use at MURR has applications including plant and sustainable cropping research. The implications of the sustainable cropping research have the potential to be significant world-wide. Increasing the sustainability and hardiness of plants means that droughts will be less catastrophic for crops and wide-spread world hunger could be decreased. A better understanding of the MURR cyclotron and the efficiency of the radioisotope production target will allow MURR to increase the amount of research that they can conduct, while decreasing the associated costs.

Plants are complex living organisms that can respond to a variety of stimuli including situations where they are in distress and at risk of being damaged or destroyed. When plants are stimulated in a threatening manner, they are able to react to defend themselves. One defense mechanism for plants is to produce chemicals intended to weaken their attacker. For example, tobacco plants produce nicotine, which is a neurotoxin for many herbivores. However, specialized caterpillars have adapted to build up nicotine in their system following tobacco leaf ingestion and, in turn, they use this as a defense against their own predators. This allows their population to increase and can lead to complete defoliation (removal of all the leaves on a plant leading to its death) of tobacco plants [2]. Therefore, chemical compound production is often not a sufficient defense for plants.

Since nitrogen and carbon are required for plant growth and reproduction, it is vital to plant well-being that they maintain healthy stores of these nutrients. Another method of plant defense is through reallocation of their critical resources in response to herbivory. If plants are attacked, it is generally their leaves that are most vulnerable to damage. For that reason, plants that are under attack will often reallocate important resources to their root systems for protection.

MURR personnel have been researching this type of nutrient reallocation through the simulation of herbivorous attacks on tomato plants. Prior to simulating an attack on the plants, ^{11}C and ^{13}N were administered to the leaves of tomato plants. A p-intrinsic-n (PIN) diode radiation detector was placed near the center of the leaves of the plant. A sodium-iodide scintillation detector was placed at the apex of the leaves and at the roots of the plant. As the radioisotopes decayed by positron emission, the detectors could observe the

emitted gamma-rays and observe the transport of nitrogen and carbon throughout the plant. To simulate plant herbivory, the plant science department uses methyl jasmonate (MeJA), which elicits similar defensive responses in plants. MeJA was misted over the leaves of the plants to simulate an attack on the leafy plant parts. As hypothesized, the plants were observed to transport the radioactive carbon and nitrogen to their root system for protection. Additionally, once the MeJA had worn off, the plants returned nutrients to their leaves. In a real attack, plants would do this to provide the carbon and nitrogen to their damaged leaves to aid in the regrowth of leaves compromised during the herbivory [2].

Similar behavior was observed in poplar tree research. [11]C was once again used as a tracer for the trees to observe nutrient reallocation in a similar experiment to those with the tomato plants [20]. Additional general research was done with ^{11}C that was used to determine the transport time of carbon through plant leaves and stems [2].

Population projections estimate that in less than 30 years the world population will increase by over 1.5 billion. In order to accommodate this growth, agriculture needs to progress with the surging population to ensure that sufficient food is available [5]. The ^{11}C and ^{13}N research at MURR is applicable to understanding the mutually beneficial relationship that exists between plants and microbes [5]. Microbiome in soil can exchange carbon and nitrogen with plants through the plant roots [5]. As a result, plants are able to grow more extensive root systems that help them to become hardened against drought and nutrient deficiency. In addition, plants would require less water and fertilization. MURR continues to research how this could be achieved through fostering a beneficial environment for rhizobacteria in the soil which will result in more efficient plant growth [5].

2.1.2 Biomedical Research

[11]C can also be used for medical research. MURR personnel have previously performed research studies to determine the effect of certain drugs on brain function [3]. Certain medications can affect production of dopamine and other chemicals within the brain. Research was done using baboons as subjects to determine whether ^{11}C-raclopride can be effectively used as a PET tracer to observe neurotransmitters [3]. The reported results have shown promising signs that this is an effective and that it may be able to be

used for humans as well to analyze the effects of drugs on human cerebral dopamine transmitters [3].

2.2 Nuclear Reactions

Nuclear reactions occur when a nucleus of an atom interacts with another nucleus or subatomic particle. The general form of a nuclear reaction is

$$a + X \rightarrow Y + b, \tag{1}$$

where X is the target nucleus, a is a sub-atomic or composite sub-atomic particle interacting with the nucleus, and b and Y represent the resultant products of the reaction. Another way to write the equation for this reaction is

$$X(a, b)Y. \tag{2}$$

There are numerous types of nuclear reactions including fusion reactions, fission reactions, and spallation reactions. More generally, nuclear reactions can be classified as direct or compound reactions. In a direct nuclear reaction, the incoming reactants interact and directly produce the outgoing products. In compound nuclear reactions, the initial reactants interact and produce an intermediate nuclide, which is in an excited state and then decays into the final reaction products [21].

The type of nuclear reaction that will occur depends on multiple conditions including the identity of the nucleus and the energy and type of incoming particle. The likelihood that a given reaction will occur in a given scenario is described by the reaction cross section. A larger cross section for a reaction corresponds to a higher likelihood of occurrence.

The nuclear primary reactions of interest for this research are $^{14}N(p,\alpha)^{11}C$, $^{65}Cu(p,n)^{65}Zn$, and $^{63}Cu(p,2n)^{62}Zn$. In the case of the $^{14}N(p,\alpha)^{11}C$ reaction, protons are accelerated into a region of ^{14}N gas where they interact with ^{14}N target nuclei to produce ^{11}C and an α particle. The $^{65}Cu(p,n)^{65}Zn$ and $^{63}Cu(p,2n)^{62}Zn$ reactions are used to characterize the proton beam. For these reactions, the proton beam is accelerated into a stack of copper foils. The relative intensity of activation products in each foil provides information about the energy of the beam incident on that foil [16].

The radioactive zinc isotopes produced within the foils decay primarily through emission of gammas of known energy. The reactions of interest that were chosen had gamma peaks that do not overlap with other gamma peaks which allows them to be identified and measured independently. Another reason these reactions of interest and associated gamma peaks were chosen is based on the cross section associated with their production is greater with respect to the other reactions that occur. This means that the peaks for the gamma peaks of interest will be larger and more discernable than for the minor reactions.

2.3 Nuclear Data

The simulations for this research required the use of evaluated nuclear data libraries that incorporate specific reaction channel cross sections. Standard nuclear cross-section libraries available in MCNP6 only allows for all possible multiplicities of a reactions to be tallied. For example, this means that any α producing reaction that takes place would be included in the resultant activity output by the simulation. However, the purpose of the simulations was to account for specific radioisotope production. Therefore, in order to measure the amount of a specific radioisotope, the MCNP6 simulations required incorporating alternate evaluated data that provided the energy dependent cross sections for the specific reaction of interest. The Java-based Nuclear Data Information System (JANIS) provided by the Nuclear Energy Agency (NEA) was used to obtain this nuclear data [15]. Figures 5-7 represent the nuclear data that is available for each reaction of interest compared to the evaluated nuclear data selected for this research.

The Figure 5(a) shows the nuclear data for the reaction of interest in the ^{11}C production model, ^{14}N(p,α)^{11}C, pulled from JANIS [15]. Figure 5(b) shows the representative cross sections that were used for this research. In this case, the experimental data, labeled as S. Takacs+ 2003 [22] and P.D. Ingalls+ 1976 [23] in Figure 5(a), had features near the threshold energy and higher energy resonances that the models did not capture. The two sets of experimental nuclear data were combined and used as one set of cross section data for the ^{11}C production simulation. The Ingalls data was used for the first three points and then the Takacs data was used for the remainder. The ENDF, TENDL and

15

JENDL models each represented the data well in some regions and were chosen to be compared with the results from the experimental data [12-14]. ENDF and TENDL use the same model for this reaction and only the ENDF data is visible since they overlap.

a)

b)

Figure 5: $^{14}N(p,\alpha)^{11}C$ reaction cross section data (a) available JANIS evaluated and experimental cross section data (b) evaluated and experimental cross section data used in this research analysis
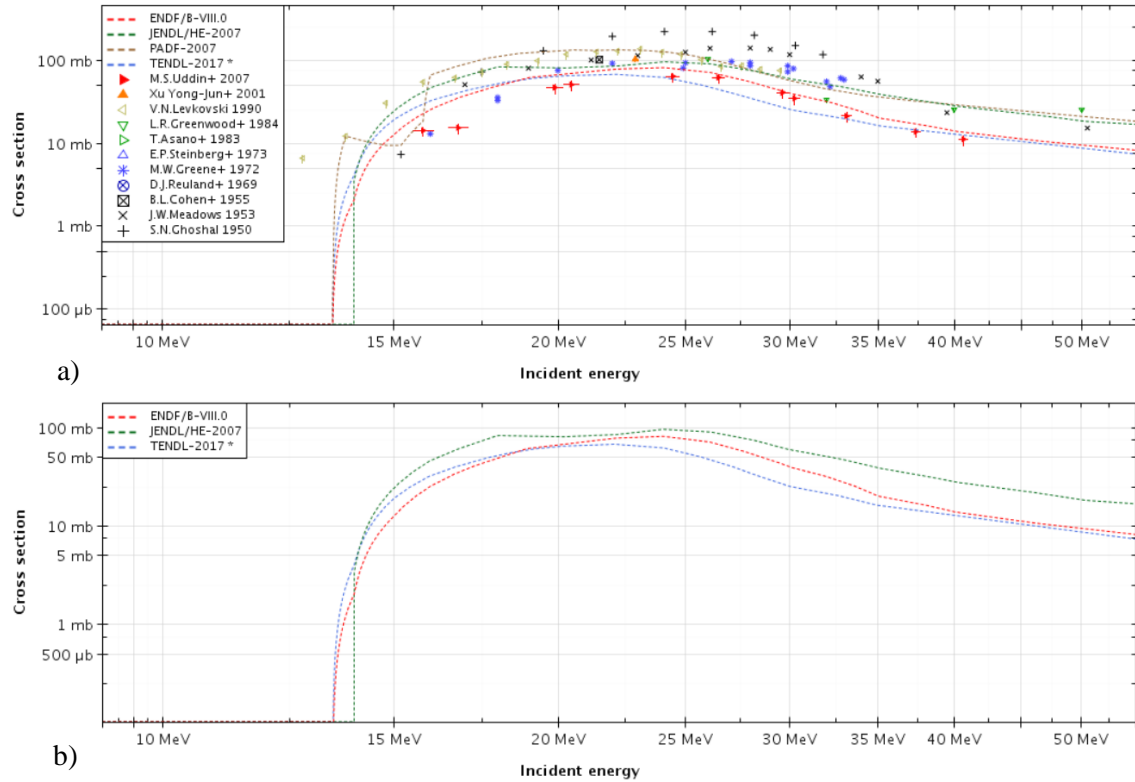
Figure 6: $^{63}Cu(p,2n)^{62}Zn$ reaction cross section data (a) available JANIS evaluated and experimental cross section data (b) evaluated and experimental cross section data used in this research analysis [20].

Figures 6 and 7 show the cross section data for the reactions of interest in the MCNP6 foil activation simulation. The first reaction of interest was $^{63}Cu(p,2n)^{62}Zn$, shown in Figure 6 For this reaction, the ENDF/B-VIII.0 [14], JENDL/HE-2007 [12] and TENDL-2017 [11] provided the best representations of the data. Figure 7(b) shows the plots for these three models which were used within the simulation and the results of each were compared. In this case, PADF-2007 [13] was not a good representation of the cross section data due to the behavior of the evaluation around 15 MeV and was not used.

Figure 7 shows the cross section data for $^{65}Cu(p,n)^{65}Zn$, which is the second reaction of interest for the foil activation simulation. For this reaction, ENDF/B-VIII.0, PADF-2007 and TENDL-2017 provided the best representations of the cross section data. In this case, JENDL/HE-2007 misrepresented the lower energies and the reaction threshold and was not used for this reaction in the foil activation simulation. JENDL cuts off at 4 MeV and drops off to zero, which is non-physical.
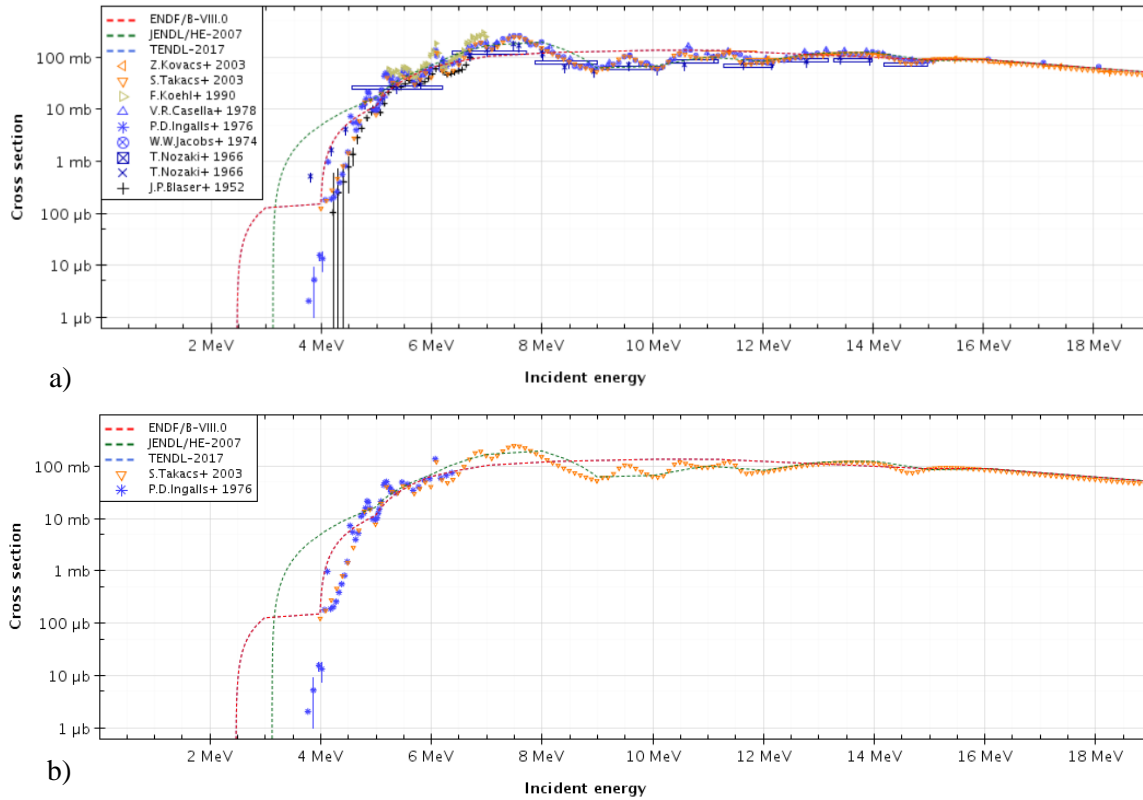
17
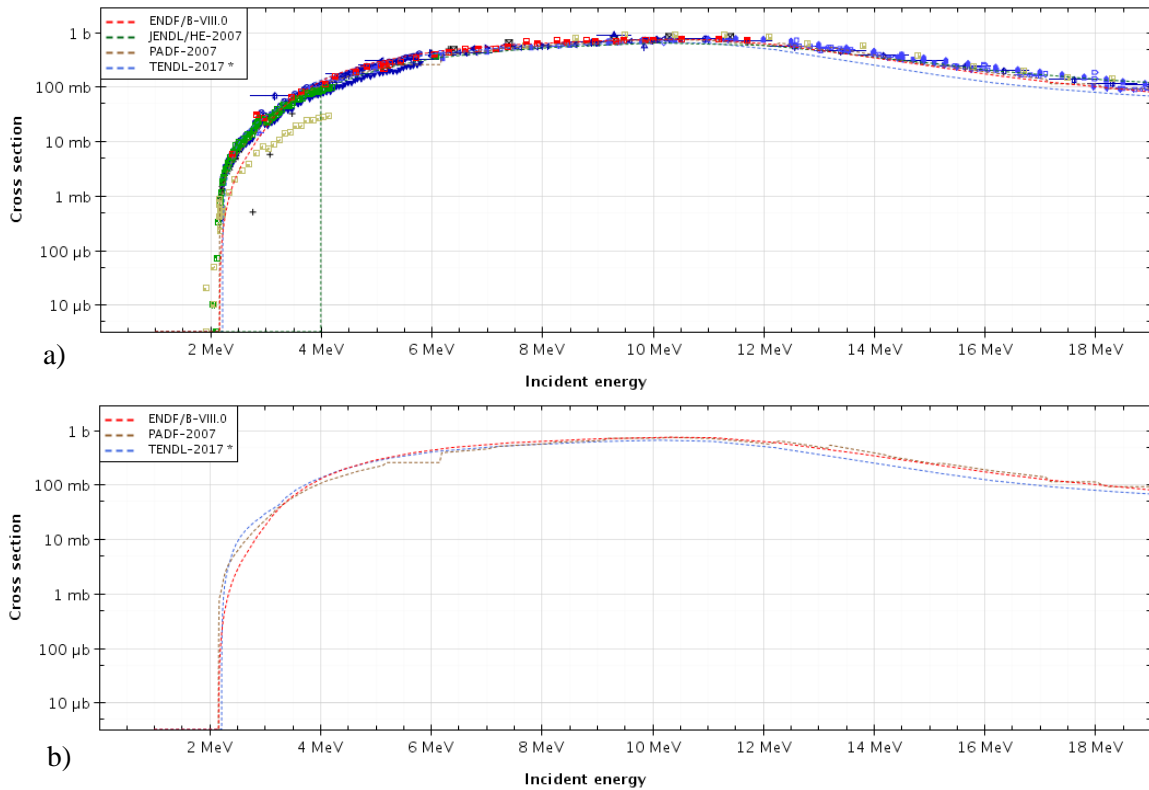
Figure 7: $^{65}Cu(p,n)^{65}Zn$ reaction cross section data (a) available JANIS evaluated and experimental cross section data (b) evaluated and experimental cross section data used in this research analysis [20].

2.4 Stacked Foil Technique

By knowing the precise energy of a cyclotron beam, operators can better understand the accurate excitation functions for radioisotope production [18]. Additionally, precise characterization of the beam allows for increased production yield efficiency through better target design [18].

One method of characterizing a cyclotron beam energy is through stacked foil activation [16]. The Department of Radiopharmaceuticals at the Nuclear Research Institute in Czechoslovakia used high-purity copper stacked foils to characterize their cyclotron proton beam. The reactions of interests for their experiments were $^{63}Cu(p,2n)^{62}Zn$, $^{65}Cu(p,n)^{65}Zn$, and $^{63}Cu(p,pn\alpha)^{58}Co$ [16]. The foils were activated via irradiation from the cyclotron proton beam and measured. Based on the results, they compared excitation

functions and data from literature for each reaction of interest. Also, reference functions were used with ratios of ^{62}Zn/^{65}Zn, ^{58}Co/^{65}Zn, and ^{58}Co/^{62}Zn in order to characterize the results [16]. The proton beam was monitored over the energy range of 13-33 MeV [16].

Australian researchers used a stack of high-purity 0.1 mm thick copper foils to measure their medical cyclotron [17]. They determined that their cyclotron beam has a precise energy of 17.49 ± 0.04 MeV. The Korean Institute of Radiological and Medical Sciences (KIRAMS) also used stacked high-purity copper foils to characterize the precise beam energy of their MC-50 cyclotron which was found to be 35 MeV [18]. For their foil activation, KIRAMS used natural copper foils and were interested in the ^{nat}Cu(p,xn)^{62}Zn and ^{nat}Cu(p,xn)^{65}Zn reactions [18].

Based on this research, it was determined that high-purity stacked copper foil activation could be used to measure the MURR PETtrace cyclotron proton beam. Multiple experiments were completed on medical cyclotrons with energies between 13-35 MeV, including two experiments that covered the anticipated energy range of the MURR cyclotron which is around 16.4 MeV [16-18].

2.5 Foil Activation Analysis

After foils are activated by radioactive beam sources, they can be analyzed by measuring them with a high-purity germanium detector (HPGe). The foils are measured individually with the HPGe detector to obtain the number of counts produced at gamma energies of interest. The radioisotopes that are produced within the foils decay by emitting gamma-rays of specific energies, which can be observed using the HPGe. In general, the foils are counted until the gamma peaks of interest have 10,000 counts or more to ensure that the statistical error associated with these energy peaks is less than 1% as the statistical error in a counting experiment is taken as the $\sqrt{N}$.

The number of counts associated with the gamma peaks of interest are used to obtain the time-zero activity of the foils, the initial activity of the foils at the end of the irradiation. This value is important because it indicates the activity that is produced during the irradiation. However, between the end of irradiation and measuring the foils, the initial

activity decays and is less intense at the time of measurement. The time-zero activity of the foils was calculated as

$$A_0 = \frac{C\lambda e^{\lambda \Delta t_j}}{(1 - e^{-\lambda \Delta t_c})\epsilon(E_\gamma)f_l I_\gamma},$$ (3)

where

A_0 is the time-zero activity,

C is the number of counts measured on the HPGe detector in the full energy peak of a given gamma peak of interest,

λ is the decay constant of the radioisotope of interest,

t_j is time between the end of irradiation and the beginning of measurement, ± 30 s due to uncertainty,

t_c is the count time for the measurement,

$\epsilon(E_\gamma)$ is the efficiency of the HPGe detector for the gamma peak of interest,

f_l is the live time fraction for the detector,

and I_γ is the gamma intensity [21].

The HPGe detector for this experiment had previously been calibrated for the efficiency at each gamma peak of interest and stand-off distance. As a result, the HPGe software, Genie™ 2000 [24], included the correction efficiency for each foil. Therefore, the $\epsilon(E_\gamma)$ term in Equation 3 was removed since it was already accounted for in the Genie 2000 reported counts.

2.6 Radiography

Radiography is a method for imaging radioactive sources. One method of computed radiography is phosphor plate imaging where phosphor plates are placed over the radioactive source to image regions of activity [25]. For this research, GE phosphor plate computed radiographic images with 100 μm resolution were used to characterize the proton beam intensity and shape. The location of the radioactive materials that result from the irradiation are visible with the radiographic images. This shows the shape and spread of

the activity and can be in turn analyzed to determine the relative intensity and shape of the beam throughout its profile.

2.7 Ion Chambers

Ionization, or ion, chambers are the simplest form of gaseous detector. They measure the effects of particles interacting in the detector gas to determine the activity of a radioactive source. The detector has an electric field that separates the charged particles created from the radiation allowing them to be collected to measure the source activity. Incident radiation within the electric field of the ion chamber directly forms ion pairs which are then measured as an electric current as they travel through the electric field of the chamber. Secondary electrons also indirectly form ion pairs. The magnitude of the source activity is proportional to the induced current [26].

A common application for ion chambers is their use to measure radioactive gases [26]. For this research, a Capintec CRC 712M ion chamber was used to measure the amount of ^{11}C that was produced in mCi during a cyclotron irradiation cycle.

2.8 Gas Density Reduction

A major operating concern in gaseous cyclotron targets is ensuring that the heat produced during irradiation is properly dissipated [19]. When the heat within the gaseous target cannot be effectively dissipated it leads to gas expansion and subsequently inconsistent density within the target. This results in less efficient operation of the production target. When cyclotrons can be operated with a higher beam current, more radioisotopes can be produced due to the increased number of interactions that can occur per unit time [19]. However, higher beam currents also lead to higher temperatures within the production target and can lead to target malfunction at high beam currents.

Another related inefficiency that can occur with gaseous radioisotope targets results from gas density reduction [19]. When the gas within the target heats up, the density goes down and the gas spreads out away from the heat source, which is generally at the center of the gas region. This results in more dense gas regions at the edges of the target which will have decreased contact with the cyclotron beam source and will decrease the overall

efficiency of radioisotope production [19]. It has been noted that convective flow occurs within the target that dissipates heat toward the walls of the target and leads to additional density reduction effects [19]. Overall, the heating and density inconsistencies throughout the target results in uneven distribution of the gas and production within the target. As a result, the radioisotope production within the target is less efficient as the beam current increases [19].

2.9 Summary

The research associated with this project required an understanding of nuclear reactions and how to specify particular nuclear reactions in MCNP6 simulations. Nuclear data was one of the key concerns for producing characteristic simulations. Another concern with these measurements was gas density reduction and beam shaping throughout the length of the production target which can affect the efficiency of production. Ion chambers can be used to measure the actual amount of ^{11}C produced which can provide experimental validation for production simulations and allow for an analysis of gas density reduction effects.

III. Simulation and Experimental Methodologies

This chapter utilizes the theory described in Chapter 2 to develop the methodologies used to characterize the proton beam, measure the ^{11}C production, and built the MCNP6 models. Section 3.1 describes the techniques used to characterize the proton beam's energy, spatial profile, and intensity profile. In Section 3.2, the development of the target model in MCNP6 is discussed. Section 3.3 discusses the ion chamber measurements used to determine the amount of ^{11}C produced during cyclotron target irradiation. In section 3.4, the target production optimization analysis methodology is described. Finally, section 3.5 discusses the statistical tests used to compare the experimental and simulation ^{11}C production results.

3.1 Proton Beam Characterization

3.1.1 Beam Energy Measurement

Stacked foil activation analysis was used to determine the energy of the cyclotron proton beam at MURR. High-purity copper foils were used for this analysis because they provide multiple reaction channels with gamma-rays that can be measured using an HPGe. The reaction channels of interest and their corresponding gamma-ray energies are: ^{63}Cu(p,2n) ^{62}Zn with $E_\gamma = 548.35$ keV and $E_\gamma = 596.97$ keV, ^{65}Cu(p,n) ^{65}Zn with $E_\gamma = 1115.5$ keV, and ^{63}Cu(p,n) ^{63}Zn with $E_\gamma = 669.6$ keV and $E_\gamma = 962.69$ keV. The ^{63}Zn peaks were not considered in the original experiment pre-planning and modeling. However, an additional foil stack irradiation was added to obtain a measurement of them during the experiment.

The design of the foil stack was determined by a foil activation simulation in MCNP6. The simulation consisted of a 16.5 MeV pencil beam source and a stack of copper foils. The foil material in MCNP6 was defined as natural copper with 69.15% ^{63}Cu and 30.85% ^{65}Cu.

The simulation was run separately with a stack of all 25 μm foils and a stack of all 100 μm foils. With the 25 μm foil stack, the full range of the beam was not captured in the foil stack. More foils could have been added, but during the physical experiment this would

have been impractical due to the time constraints associated with the execution of the HPGe counting. The simulation was also run with all 100 μm foils. However, this configuration did not capture the ^{62}Zn in more than the first foil.

The simulation was re-run with different arrangements of 25 and 100 μm foils until it captured each of the isotope activity profiles. The primary objectives were to obtain higher resolution at the regions of peak production for each isotope using thinner foils and to avoid large jumps in the relative activity per foil by including thinner foils in those areas. The final arrangement that was chosen included a mixture of 25 and 100 μm foils as shown in Figure 8 and Figure 9. Figure 8 shows the chosen foil arrangement and the normalized results of the MCNP6 foil activation simulation for ^{62}Zn. The first three 25 μm foils were primarily intended to capture the ^{62}Zn activity since it drops off very quickly in the foil stack due to a high reaction energy threshold. The energy threshold for a reaction is the minimum amount of energy that is required for that reaction to occur.
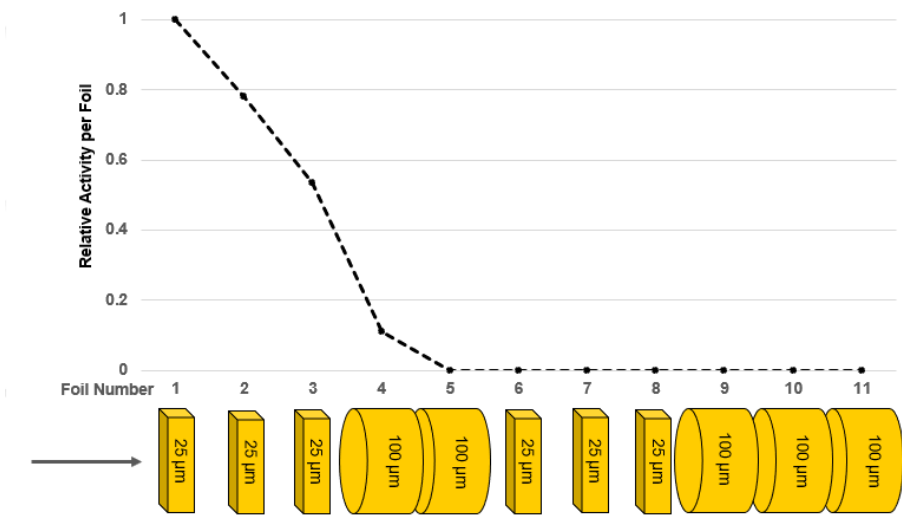
Figure 8: Normalized ^{62}Zn activity per foil based on MCNP6 foil activation simulation. The line is included to guide the eye.

Figure 9 shows the results of the MCNP6 simulation for ^{65}Zn activity per foil. The 6th through 8th thinner foils were intended to capture the peak of the ^{65}Zn activity. The foil stack shown in Figures 8 and 9 was the arrangement used in the stacked foil activation

experiments. However, only the first ten foils were measured using the HPGe since the eleventh foil consistently did not have measurable activity.
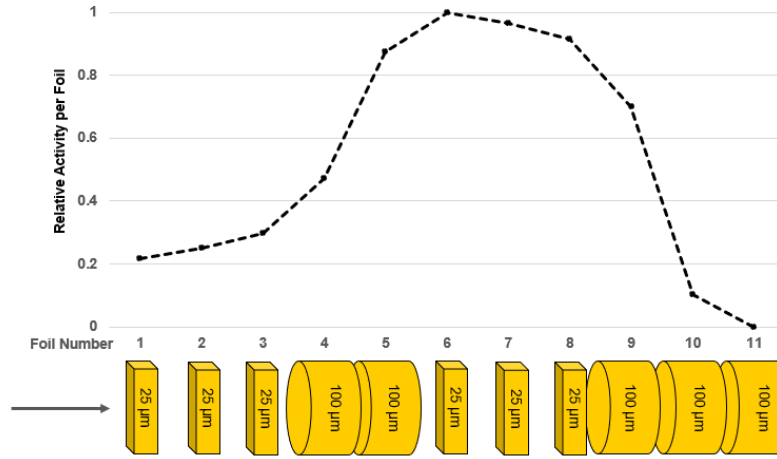
Figure 9: Normalized ⁶⁵Zn activity per foil based on MCNP6 foil activation simulation. The line is included to guide the eye.

The foils were stacked and taped together at the sides. The tape did not obstruct the beam of the cyclotron from interacting with the foils. Three foil stacks with the same orientation were created. Each foil stack was placed directly in contact with the target window and irradiated by the cyclotron as shown in Figure 10.

(a)   (b)
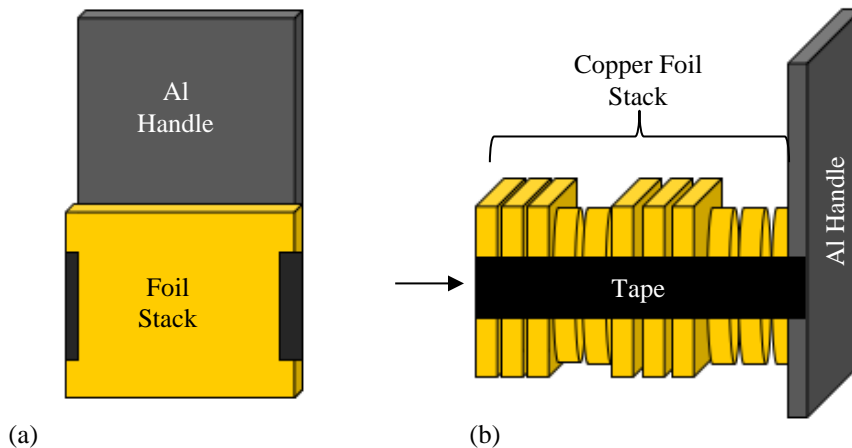
Figure 10: Foil stack (a) front view and (b) profile. The aluminum handle was used for placing and extracting the foil stack from the cyclotron irradiation position. The tape was used to hold the foils together but did not obstruct the beam.

25

The first and third foil stacks were each irradiated for 30 s with a cyclotron beam of 5 μA. The second foil stack was irradiated for 30 min with a cyclotron beam of 5 μA. The first foil stack was used as a test case and measured with an ion chamber to get an estimate of the activity in each foil.

The goal for the 30 min irradiation was to produce larger amounts of ^{65}Zn within the foils. ^{65}Zn has a half-life of 243.66 days and takes longer to reach saturation activity within the foils. A 30 min irradiation does not reach saturation but ensured that an appreciable amount of ^{65}Zn was produced. The drawback to the longer irradiation was that it was more highly radioactive and required approximately 6-10 hours of additional cooling time prior to measurement. The cooling time was necessary to count the foils with a reasonable detector dead time, <10%. ^{62}Zn and ^{63}Zn have short half-lives, (9.186 h and 38.47 min, respectively) and decayed significantly during the cooling time of the foils. The 30 s irradiation captured the shorter-lived isotopes by allowing for the foils to be counted with less cooling time.

After the foils were irradiated, they were allowed to decay for approximately 20 hours for the 30 min irradiation and 1.5 hours for the 30 s irradiation. The decay time was based on a variety of factors including some limitations based on safety considerations and MURR operating procedures. The activity of the foils was measured by MURR personnel to ensure it was safe to be transported from the cyclotron to the HPGe laboratory. The HPGe specifications can be found in Appendix A.

Each foil was counted until the gamma-ray lines of interest had 10,000 counts in the full energy peak. The counting times per foil ranged from approximately 15 min to 3 hours. In the case of the 30 s irradiation, the foil measurements had to be performed quickly in order to prevent all of the activity from decaying away before they could be measured. Therefore, in some cases, only 5000 counts were obtained in some of the full energy peaks for ^{63}Zn.

3.1.2 Beam Profile Measurement

After the foil HPGe measurements were complete, the first foil stack that was irradiated for 30 min was imaged using a General Electric Imaging Plate Unit (IPU) radiographic system to determine the beam spread and intensity profile. The radiographic

images were taken by placing a phosphor plate over the spread-out foils. Figure 11 shows the radiographic images obtained. In Figure 11, the arrow on the top diagram represents the proton beam direction of flow through the stack. A diagram of the foil stack arrangement showing the thickness and shape for each foil for comparison with the radiographic images is also included in Figure 11.
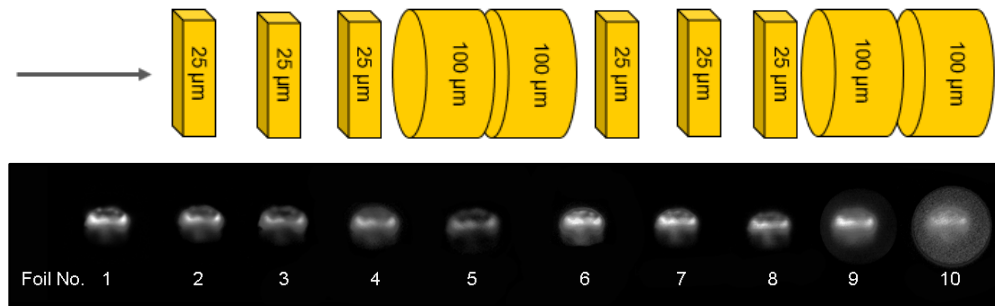
Figure 11: Radiographic images of the 30 min irradiated foils with a diagram of the foil thicknesses and shapes for comparison.

The foil stack was allowed to decay for approximately 3 days prior to taking these images. The short-lived isotopes, primarily ^{62}Zn and ^{63}Zn, produced in the foils resulted in the images becoming over-exposed if the images were taken too quickly post-irradiation. After a few days, the short-lived isotopes had decayed away enough to successfully image the foils. The exposure time was adjusted between the foils in order to get consistent images that could be compared.

3.2 ^{11}C Production Simulation

The MURR ^{11}C production was simulated in MCNP6 and compared with experimental results. The updated beam profile and beam energy of 14.7 MeV based on experimental data were included in the production simulation.

The ^{11}C target was modeled in accordance with GE specifications as shown in Figure 12. Only the gas rear flange head piece, target body, and gas region were modeled as these are the only components where the proton beam would interact. The base of the target was modeled as an aluminum rectangle with a cylindrical hole in the center. The head piece was also modeled as an aluminum rectangle connected to the base at one end.

27

The other end of the base is connected to a Havar® foil window. Havar® foils are cobalt-based alloy foils designed to be used in high temperature environments The Havar® foil window consisted of one 25 μm thick Havar® foil on either side of a 1.5 cm thick region of helium used for cooling the foils.
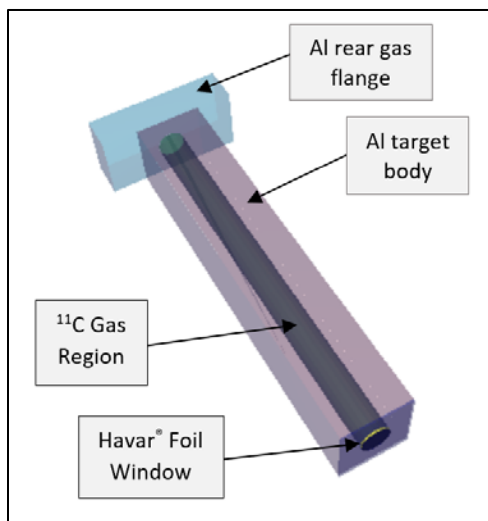
Figure 12: ^{11}C production target model in MCNP6 shown in Visual Editor (VISED). The components are transparent in the image with the exception of the Havar® foil window to show the interior target geometry.

The pressure in the He cooling region was 50 psi. The foil window is designed to allow the beam to pass through while maintaining the desired high pressure required within the target fill gas and the vacuum in the cyclotron. The pressure of the ^{14}N fill gas was set to 165 psi for ^{11}C production.

3.3 Ion Chamber Measurements

In order to benchmark the ^{11}C production simulation, ^{11}C production was measured with a Capintec Radioisotope Calibrator (CRC-712MV) ion chamber. Production cycles were run with the following beam currents: 5 μA, 10 μA, 20 μA, 30 μA, and 40 μA. The beam current strength has an approximately ±1 μA uncertainty. The irradiation time was set for 5 min for each of the cycles; however, the cyclotron tunes during that time as well. The target gas was filled to an initial pressure of 165 psi with a gas density of 0.0131 g/cc. There is uncertainty associated with the tune time and the precise amount of time that the

cyclotron runs following the tuning period. Therefore, the run time for each production cycle was approximated as 4.75 ± 0.25 min.

Once each production cycle was run, the gas in the target was evacuated to a 5 Å Ascarite II NaOH coated SiO_2 chemical trap which collects CO_2. The chemical trap had an efficiency of greater than 0.99 for collecting CO_2. The carbon that is collected by the chemical trap includes the ^{11}C, which is the product of interest. ^{13}N, ^{14}O, and ^{15}O are also trapped in the chemical trap. MURR personnel indicated that the trapping efficiency is relatively low for ^{13}N, but it is higher for the oxygen isotopes. The specific activity, reported in mCi by the ion chamber, was measured beginning 1 min after the end of irradiation through 45 min post-irradiation. For the first 10 min, the specific activity was observed every minute; between 10-45 min, measurements were taken every 5 min. Multiple measurements were taken in order to observe the radioactive decay of the isotopes produced and to determine the activity at the end of irradiation.

3.4 ^{11}C Production Target Optimization

The ^{11}C production target at MURR is a standard GE target and is designed generally for radioisotope production but not specifically for ^{11}C production. One concern with production efficiency is related to beam spreading that occurs with the cyclotron beam. As the beam is directed down the gas region of the target it spreads out. Prior to this research MURR personnel hypothesized that by the end of the target it likely reaches a width that exceeds that of the target gas region leading to energy from the beam being lost to irradiation of the metal sides of the target.

In order to analyze the effects of the beam-spread within the production target, a mesh tally was employed in the MCNP6 simulation. The mesh tally enables accounting of the proton beam flux to be observed throughout the length and width of the production target to determine where the beam hits the target walls and whether the target gas fully stops the beam. The mesh tally extends into the sides and the far end of the target to determine whether beam interactions occur within the target walls. If the proton beam interacts with the walls or the back of the target, efficiency is lost. Analyzing the production

within the ^{11}C target and identifying any inefficiencies is important to understanding what an optimal production target looks like and determining the ideal operating conditions.

3.5 Statistical Tests

Experimental and computational results can be statistically compared using chi-squared and Kolmogorov-Smirnov (KS) statistics [27] [28]. Both of these tests help to determine how well the computational results match the experimental results in order to experimentally validate the simulations.

The KS statistic is used to determine whether two sample sets come from the same distribution [27]. The test calculates a KS statistic and a p-value which determine whether the null hypothesis, that the two samples come from the same distribution, can be rejected or not [27]. When the p-value is high it means that the null hypothesis fails to be rejected [27].

One limitation to this test is that it does not have a high-discrimination index. The test can result in high p-values and identical p-values for different sample sets. Therefore, the test does not always give a definite result when comparing different sample sets.

The chi-squared statistic is another form of hypothesis testing which determines whether there are considerable differences between two sample sets. In this case, the chi-squared result must be small in order to indicate that the two sample sets are alike [28]. Equation 3 is the equation to calculate the chi-squared statistic,

$$\chi^2 = \sum \frac{(Exp - Obs)^2}{Exp}, \tag{4}$$

where *Exp* are the experimental results, *Obs* are the observed, experimental values. This equation outputs a number rather than a p-value and the objective is to get the lowest number [28]. By using the χ^2 value rather than the p-value associated with it, the test is more discriminating and can give a definite result about the likenesses between the sample sets.

IV. Analysis and Results

This chapter utilizes the methodology described in Chapter 3 to characterize the cyclotron proton beam, to analyze its effects on simulation results, and to compare experimental and simulation results for the ^{11}C production. In section 4.1, the results of the proton beam characterization are reported. In Section 4.2, the results of the target model in MCNP6 are discussed. Section 4.3 discusses the ^{11}C ion chamber results and compares those results to the MCNP6 simulation results. Finally, in section 4.4, the target production optimization analysis is discussed.

4.1 Proton Beam Energy Measurement Results

The MURR cyclotron beam energy was measured using stacked foil activation as described in Section 3.1.1. Each foil's activity was measured with an HPGe detector. The resulting gamma-ray pulse height spectra were analyzed to calculate the time-zero activity, defined as the initial activity of the foils at the end of the irradiation. This value is the value that will be directly compared to the modeling results. Equation 3 from section 2.5 was used to calculate the time-zero activity.

The copper foils used to measure the cyclotron beam energy produced zinc isotopes when irradiated with the proton beam. The zinc isotopes of interest for this project were ^{62}Zn, ^{63}Zn, and ^{65}Zn. However, the ^{63}Zn results ended up being rejected due to significant coincidence summing concerns. This isotope has a large number of coincident gammas associated with each of their primary gamma energies. As such, there is a considerable amount of uncertainty in the results of these measurements. ^{63}Zn has a half-life of 38.47 min, so the foil stacks required being counted quickly after the irradiation in order observe the ^{63}Zn. In order to increase the efficiency of the foil counting to accommodate this, the foils were counted as close to the HPGe detector as possible while keeping the dead time within reasonable limits. The issue with this methodology is that it exacerbates coincidence summing issues. Coincidence summing effects increase based on the inverse square of the distance between the detector and the source being measured. Therefore, at close distances the counts lost to coincidence summing increase drastically.

The HPGe had a plastic stand that fit over the crystal with detection positions from 1 to 10 cm above the detector face. Locations 1-3, 5, and 10 were all calibrated by MURR personnel 3 days before the experiments and were used throughout the measurements. To minimize dead time and efficiently measure all of the foils before considerable activity decayed away, the detection location was adjusted throughout the measurements. This required an additional factor to be included in the calculations to account for the solid angle of the foils. The foils were analyzed as if they were point sources, but closer detection locations cannot be accurately considered point sources. The point and volume source solid angle were compared for each of the measurement locations. Although the largest difference was seen at the closest locations, there was a difference between point and volume source solid angles even at 10 cm. The point source solid angle was calculated as

$$\Omega \cong N \frac{\pi a^2}{d^2}, \tag{5}$$

where N is the number of counts, d is the distance from the detector and a is the detector radius [9]. If the source cannot be considered a point source, then Equations 6 through 10 must be used, where s is the source radius [9].

$$\alpha = \left(\frac{a}{d}\right)^2 \tag{6}$$

$$\beta = \left(\frac{s}{d}\right)^2 \tag{7}$$

$$F1 = \frac{5}{16} \frac{\beta}{(1+\beta)^{7/2}} - \frac{35}{16} \frac{\beta^2}{(1+\beta)^{9/2}} \tag{8}$$

$$F2 = \frac{35}{128} \frac{\beta}{(1+\beta)^{9/2}} - \frac{315}{256} \frac{\beta^2}{(1+\beta)^{11/2}} + \frac{1155}{1024} \frac{\beta^2}{(1+\beta)^{13/2}} \tag{9}$$

$$\Omega \cong 2\pi \left[1 - \frac{1}{(1+\beta)^{1/2}} - \frac{3}{8} \frac{\alpha\beta}{(1+\beta)^{5/2}} + \alpha^2[F1] - \alpha^3[F2] \right] \tag{10}$$

The point source solid angles were divided by the volume source solid angles for each of the detection positions and the corresponding factors were multiplied by each of the time-zero activities.

The relative intensity for the foil stack was reported based on averaging the intensities of the experimental results for each foil, normalizing the averaged data, and reporting the single average relative intensity for each foil position in the overall stack. These results were compared to the relative intensities of each foil modeled with the foil

activation MCNP6 simulation. The simulation was run with cross section data from TENDL, ENDF, and JENDL for the ^{62}Zn analysis and TENDL, ENDF, and PADF for the ^{65}Zn analysis. Tabular cross section data from each library was pulled from JANIS [15].

To compare the simulation and experimental results, a Kolmogorov-Smirnov (KS) statistic and a chi-squared (χ^2) statistic were both used [27]. The goal of each of these statistics is to determine whether the experimental and simulation results came from the same distribution [28]. A Python 3.6 code was used to iterate the statistical analyses over a range of simulated beam energies to determine the most likely beam energy.

The MCNP6 foil model was run with varying beam energy values from 13.5 to 16.9 MeV to generate activity profiles for ^{62}Zn and ^{65}Zn with cross section data from each of the given libraries. Next, the modeled results were compared to the experimental results using the KS and χ^2 statistics. The code was iterated at each beam current until the best solution was reached for each of the cross-section libraries for ^{62}Zn and ^{65}Zn.

The results for the KS statistic were consistent; however, they indicated that the KS statistic does not have a high discrimination index since there is a wide range of energy values that give the same or very similar p-values. Therefore, only χ^2, Equation 4, was used in the final analysis since it provided more discrimination between the beam energy values. For the χ^2 statistic, the objective is to get the lowest number.

Figure 13 shows the plots for ^{62}Zn based on the simulated beam energy that gave the best chi-squared results when comparing the experimental results to the simulation results with TENDL, ENDF, and JENDL cross section data. The vertical error bars are less than 0.3% for each of these measurements. The foil depth location of each point represents the midpoint depth of the foil and the horizontal error bars show the thickness of the foil.
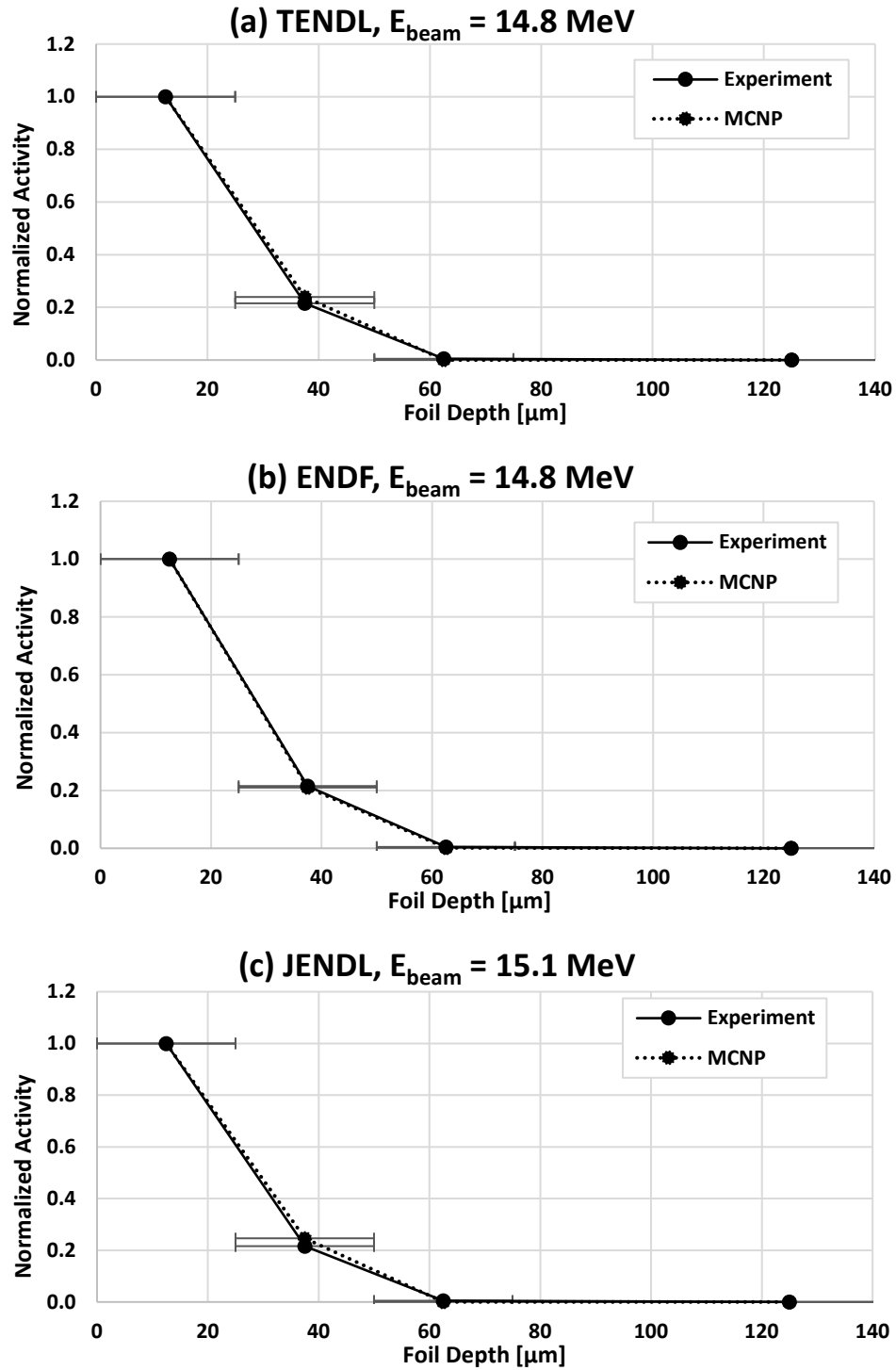
Figure 13: Normalized ^{62}Zn experimental compared to MCNP6 activity results using (a) TENDL cross-section data and beam energy of 14.8 MeV, (b) ENDF cross section data and beam energy of 14.8 MeV, and (c) JENDL cross section data and beam energy of 15.1 MeV.

Figure 14 shows a comparison of the χ^2 values obtained comparing the ^{62}Zn experimental and simulated results for the model incident beam energies.
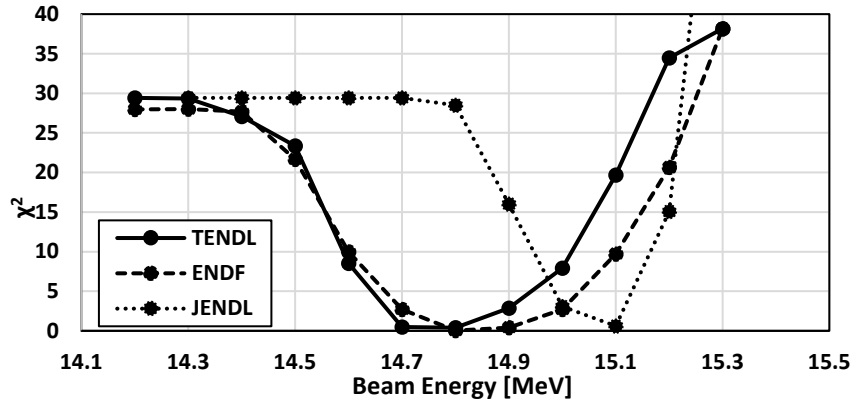

Figure 14: χ^2 values comparing ^{62}Zn experimental and MCNP6 results versus beam energy of simulation.

Each of the cross section result sets have a well-defined valley which represents the most likely energy value for the beam. The ENDF and TENDL results match up very closely and agree the most likely energy for the cyclotron beam is 14.8 MeV. The JENDL data do not match up with the other two and predicts a value of 15.1 MeV. The reason for the plateau for the JENDL data is because of an anomaly at the threshold energy. As shown in Figure 6, the JENDL cross section data for ^{62}Zn production drops down to zero suddenly, which is not realistic cross-section behavior. Additionally, the reaction threshold was calculated to be 13.48 MeV using the National Nuclear Data Center Q-value calculation tool [34]. The ENDF and TENDL cross section library thresholds agree with this calculated value. JENDL does not agree with this and instead has a reaction threshold of 14.0 MeV. Although this is a small difference in the threshold energy, it has a large impact in this case. The cyclotron beam energy is not much greater than this threshold energy so even a small increase in the threshold energy has a large effect on which foils are expected to have ^{62}Zn produced within them based on the simulation. Based on this, the JENDL results were rejected since they did not represent the threshold as well. The ^{62}Zn results, excluding the JENDL results, were averaged and the standard deviation was calculated to determine that the beam energy is 14.8 MeV.

Figure 15 shows the plots for ^{65}Zn based on the χ^2 minimization comparing the experimental to the simulation results cross-section data.
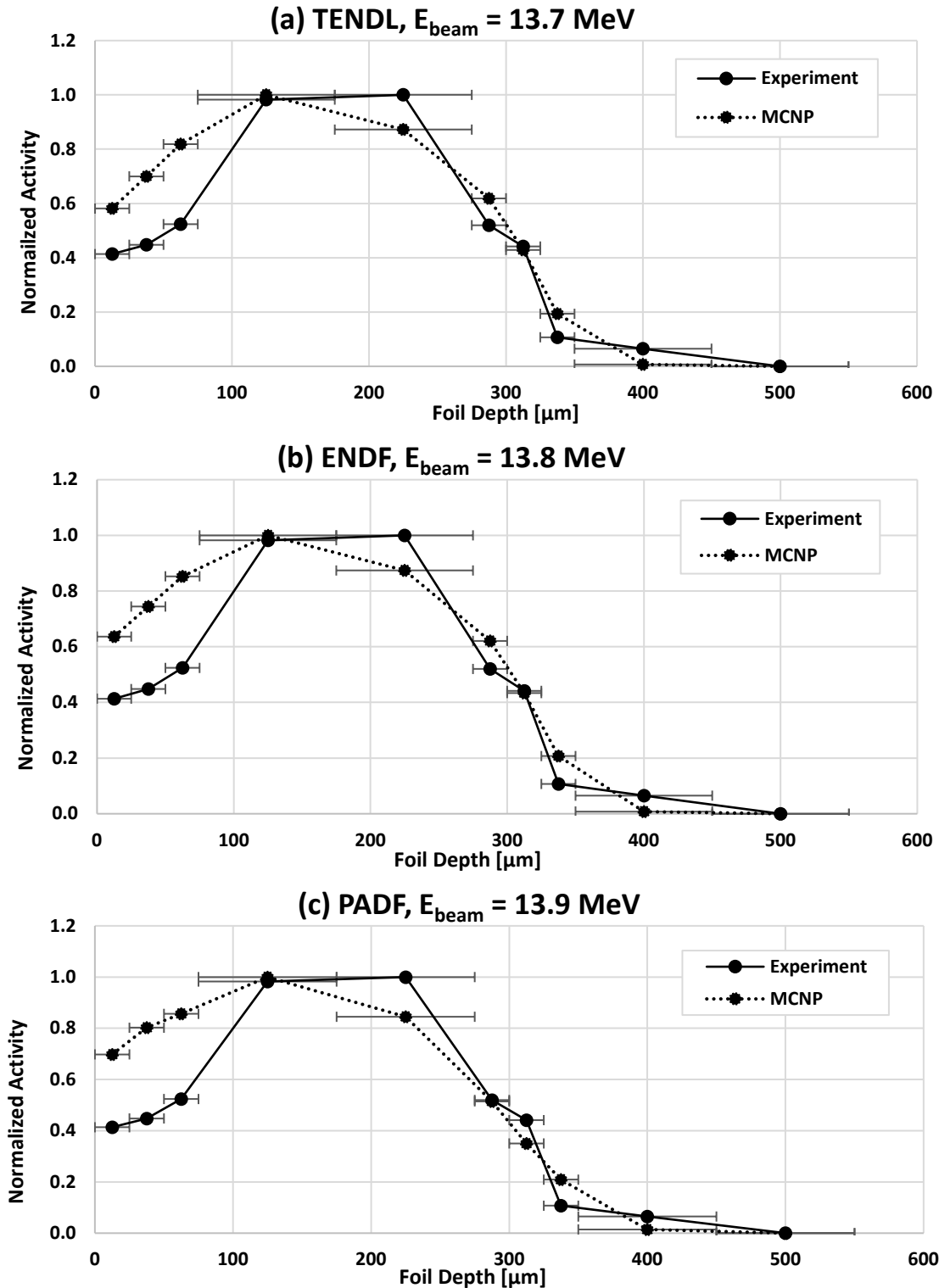
35

Figure 15: Normalized ^{65}Zn experimental compared to MCNP6 simulation results using (a) TENDL cross section data with beam energy of 13.7 MeV, (b) ENDF cross section data with a beam energy of 13.8 MeV, (c) PADF cross section data with a beam energy of 13.9 MeV.

Figure 16 shows a comparison of the χ^2 values obtained comparing the ^{65}Zn experimental and simulated results for the incident beam energies considered in the model. The beam energy with the lowest χ^2 value is much lower than the results for ^{62}Zn. The PADF results indicate a beam energy of 13.9 MeV, the ENDF results indicate 13.8 MeV, and the TENDL results indicate 13.7 MeV.
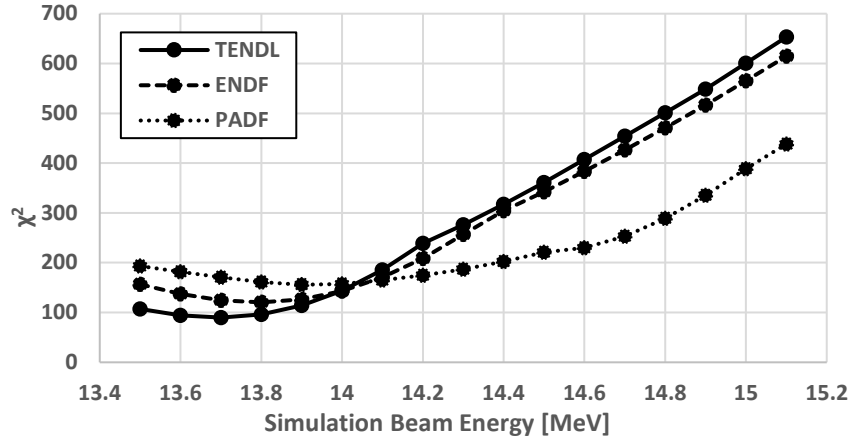

Figure 16: χ^2 comparing ^{65}Zn experimental results and MCNP6 versus beam energy of simulation.

In addition to disagreeing with the ^{62}Zn data, the results with the lowest χ^2 values are also approximately equal to the reaction energy threshold for ^{62}Zn production which is 13.48 MeV. If the proton beam energy were that low, then ^{62}Zn would likely not be produced in the foils. Additionally, as observed in Figure 15, the results at these beam energies do not accurately capture the peak of the ^{65}Zn production. The simulation results appear to peak before the experimental results which indicates that the simulation energy is likely lower than the actual beam. The two peak values and the ninth and tenth foils are all 100 μm thick compared to the other foils which are 25 μm thick foils. During the χ^2 analysis it was noted that at a slightly higher beam energy, the peak values were matched very closely, and the simulation results were more centered about the peaks. These results indicated that there is likely a yet to be determined correction factor for the thin foils which are consistently depressed compared to the experimental values for these foils. Therefore, another analysis was done using only the two peak values to determine which beam energies gave the best results for the peak values. This analysis attempted to compensate

for the depressed activity in the small foils. Figures 17 shows the χ^2 minimization results for the peak analysis for ^{65}Zn.
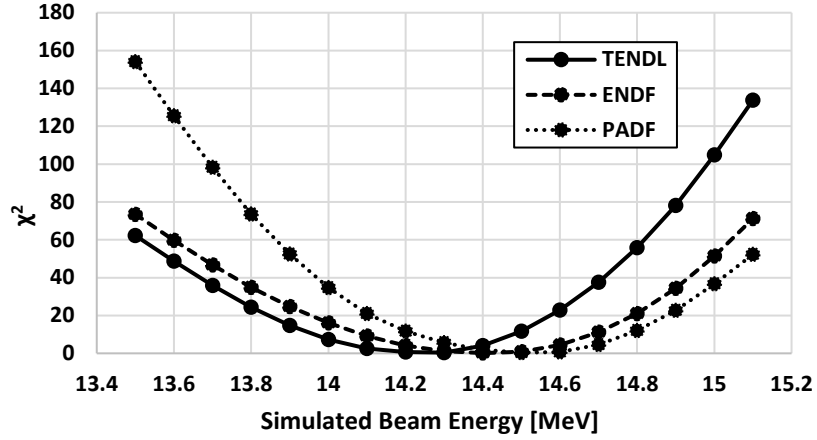
Figure 17: χ^2 comparing ^{65}Zn peak experimental and MCNP6 results versus beam energy of simulation.

Figure 18 shows the best simulated energy results for each cross section library compared to the experimental results based on the peak χ^2 minimization analysis.
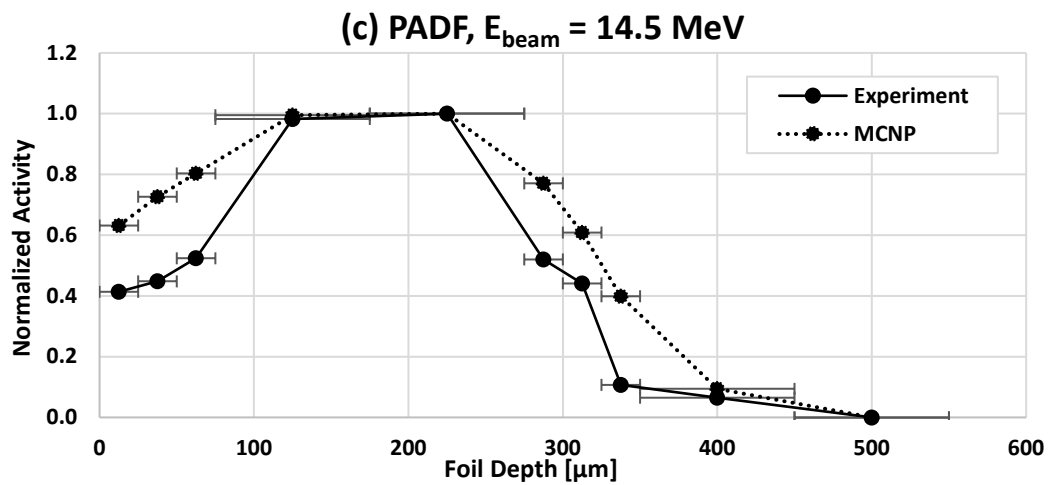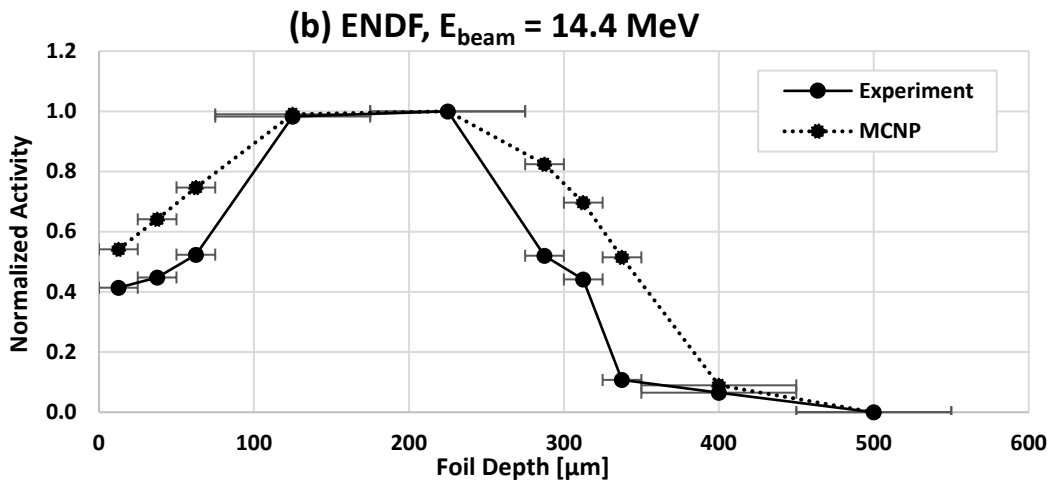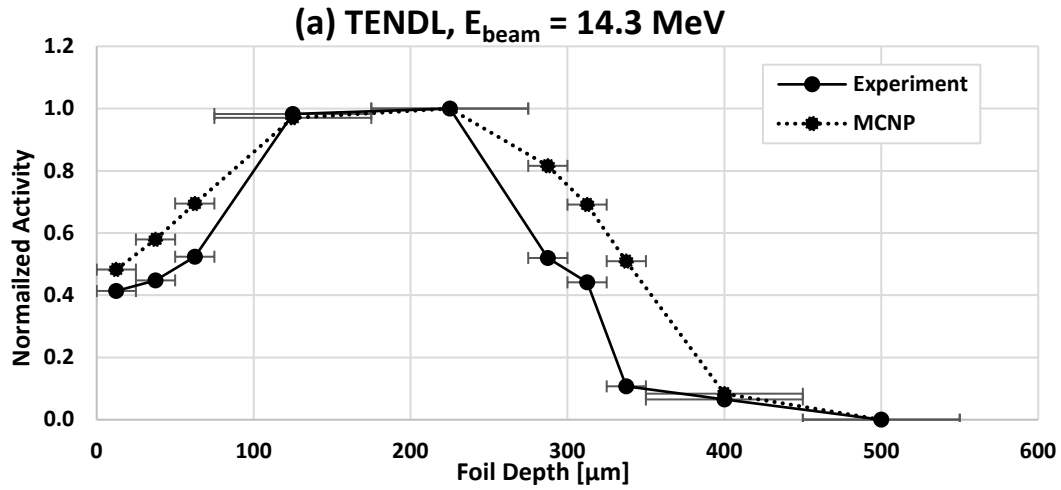
Figure 18: Normalized ^{65}Zn experimental compared to MCNP6 simulation results, showing the best match for the peak of the spectra using (a) TENDL cross section data with beam energy of 14.3 MeV and (b) ENDF data with a beam energy of 14.4 MeV and (c) PADF data with a beam energy of 14.5 MeV.

The peak χ^2 analysis for ^{65}Zn, which leads to Figure 17, only compared the two peak foil values for the experimental compared to the simulation results. Rather than trying to match the value for every foil, this analysis only calculated the χ^2 value based on comparing the amount of ^{65}Zn in the two foils with the peak values. Figure 18 demonstrates that the given beam energies represent the data very well at the peak values and the last two foils which are all 100 μm foils. Whereas for the other foils, which are 25 μm foils, there is a consistent offset from the experimental values. These results agree more closely with the ^{62}Zn results and are in better agreement with the observed ^{62}Zn and the energy threshold for the reaction.

One possible reason for the misalignment with the χ^2 minimization results is that the foils that represent the peak values for the experimental results were both 100 μm foils, whereas the ones on either side are 25 μm foils. The 25 μm foil results (1-3 and 6-8) are consistently lower compared to the simulated results while the 100 μm foil results (4, 5, 9, and 10) match well. There is evidence to indicate that the 25 μm foils may have a correction factor that has been neglected or miscalculated. One possible explanation for this discrepancy is that the thin and thick foils have different relative contributions from hot ion recoil from neighboring foils. The product nuclei (^{62}Zn or ^{65}Zn) can recoil from one foil into another neighboring foil. This has a larger impact in thinner foils where the relative amount of the product nuclei loss is increased. This phenomenon was not explored further in this research, but it provides a possible explanation for the discrepancies between the 25 and 100 μm foils.

Overall, the ^{62}Zn result indicate that the beam energy is 14.8 MeV. Considering the peak analysis for the ^{65}Zn results, the beam energy is most likely 14.4 MeV. The beam energy of the cyclotron has therefore been determined to be 14.6 ± 0.2 MeV by averaging the most representative two ^{62}Zn results (TENDL, ENDF) and three ^{65}Zn results (TENDL, ENDF, PADF) and taking the standard deviation.

4.2 ^{11}C Production Simulation in MCNP6 Results

MURR ^{11}C production was simulated in MCNP6 with ENDF, JENDL and experimental cross section data obtained from JANIS [15]. Results using each of the cross

section libraries were tallied and compared. The initial tally values were given in reactions per source particle per unit volume. The simulation was initially run with both a mono-directional point source proton beam and then run with an updated beam energy and intensity profile obtained from the analysis of the activated foil analysis.

The beam profile was determined based upon stacked foil radiographic images. Figure 19 shows a histogram of the beam intensity profile. The beam intensity profile was included in the final MCNP6 simulation using intensity bins.
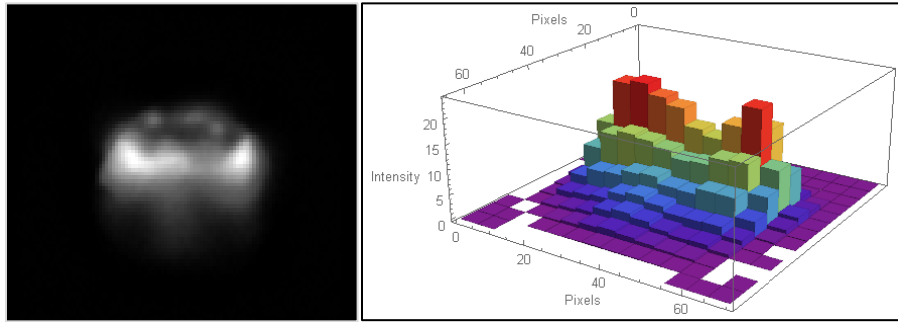
Figure 19: Beam intensity profile obtained from the analysis of foil 1. (Left) shows the first foil radiographic image and (right) shows the beam intensity profile that was produced from the left image.

To determine the effect of updating the beam definition, the simulation was run with the original 16.4 MeV mono-directional point source and the updated 14.6 MeV beam profile source. Table 1 shows the tally results for each set of cross section data with the two source definitions.

Table 1: ^{11}C production model results based for each set of cross section data and source definition.

Cross-Section Data Source	16.4 MeV Mono-directional Point Beam Source $\left[\frac{rx}{src-cm^3}\right]$	14.6 MeV Characterized Beam Source $\left[\frac{rx}{src-cm^3}\right]$
Tabulated Experimental Library	1.36×10^{-2}	1.14×10^{-2}
ENDF	1.50×10^{-2}	1.29×10^{-2}
JENDL	1.42×10^{-2}	1.18×10^{-2}

The average difference between the old and updated source profile results was approximately 15.8%. The simulated irradiation ^{14}N gas conditions were based on nominal density at a pressure of 165 psi and temperature of 20°C.

41

The tally output from the MCNP6 simulation was in reactions per source particle, per volume. The results were then converted to mCi to compare the simulation results with the experimental results using Equation 11. Equation 12 was used to convert the reaction rate from the simulation tally to the time zero activity [21].

$$\dot{R} = t_m I_{beam} \frac{1}{Q_p} V_t \tag{11}$$

$$A_0 = \dot{R}\left(1 - e^{-\lambda_0 t}\right) \tag{12}$$

In Equations 11 and 12, $\dot{R}$ is the reaction rate, t_m is the MCNP6 tally result, I_{beam} is the beam current, Q_p is the proton charge, V_t is the target gas region volume, A_0 is the initial activity of ^{11}C produced in the target, λ_0 is the ^{11}C decay constant, and t is the irradiation time. The irradiation time was taken from the experimental procedures in order to replicate what was obtained in the experimental data to allow for comparison between the values. The results were then normalized by irradiation time and beam current to obtain an activity per unit charge. Table 2 shows the time-zero activity (A_0) results of the ^{11}C production simulation.

Table 2: ^{11}C production simulation results for each cross-section data set.

Cross-Section Data Source	A_0 [mCi/(μA-s)]
Tabulated Experimental Library	1.67
ENDF	1.90
JENDL	1.73

4.3 Ion Chamber and Experimental Validation Results

The amount of ^{11}C produced with the MURR cyclotron was measured using an ion chamber. Production cycles were run with 5 μA, 10 μA, 20 μA, 30 μA, and 40 μA beam currents with an uncertainty $\pm$ 1 μA for each. Each production run was for 4.75 $\pm$ 0.25 min. After the irradiation was complete, the activity was obtained from the ion chamber every 1 min for the first 10 min and every 5 min after that out to 45 min. Figure 20 displays the natural log of the measured activity from the ion chamber measurements versus the time for the 10 μA production cycle.
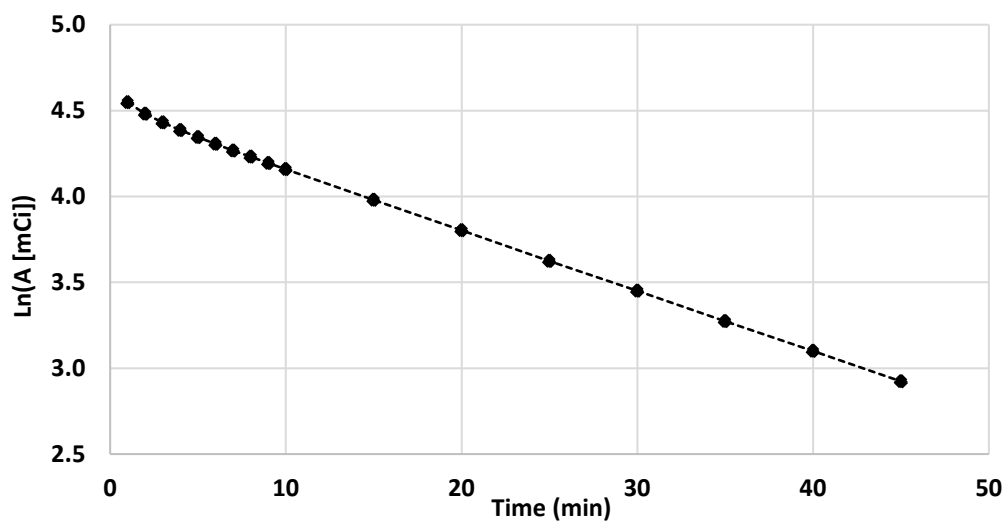
Figure 20: ^{11}C production ion chamber activity measurements. The dashed line is intended to guide the eye.

The natural log of radioisotope activity is expected to be linearly decreasing with time, and the slope is equal to half-life of the radioisotope. As observed in the plot in Figure 20, the first data points do not follow the expected linear relationship. This is due to ^{11}C not being the only radioisotope that is produced during proton irradiation of ^{14}N gas. In addition to ^{11}C, ^{13}N, ^{14}O, and ^{15}O are also produced.

Of the radioisotopes that are produced, ^{11}C is the longest-lived with a half-life of 20.334 min. ^{13}N has a half-life of 9.965 min, ^{14}O has a half-life of 122.24 s, and ^{15}O has a half-life of 70.598 s. The Ascarite chemical trap in the ion chamber collects ^{11}C in the form of CO_2 very effectively with an efficiency of approximately 99.9%. ^{14}O and ^{15}O are also collected in the trap in the CO_2. ^{13}N is not collected as efficiently. In order to only account for the activity produced by the ^{11}C, only the data beginning at 20 min was used in the production analysis. By 20 min, the ^{15}O and ^{14}O have decayed through roughly 10 and 20 half-lives, respectively, which means that they are effectively absent from the data. The ^{13}N has decayed through roughly two half-lives. Given that it also was not collected as effectively by the ion chamber trap, its effects on the measured activity are minimized.

To demonstrate the effect of only using the data after 20 min, an analysis was done on the half-life calculated for the data sets for each of the beam currents. The results of the

half-life calculations are shown in Table 3 comparing calculations done with all the data versus only the data after 20 min.

Table 3: Half-life calculations for ^{11}C results for each beam current data set, comparing calculations used with all the results versus the corrected data sets using results from 20-45 min.

		5 µA	
^{11}C Half-life	20.33 min	^{11}C	18.97 min *(0.93)*
		^{11}C (Corrected)	**20.05 min** *(0.99)*
10 µA		**20 µA**	
^{11}C	18.33 min *(0.90)*	^{11}C	17.64 min *(0.87)*
^{11}C (Corrected)	**19.66 min** *(0.97)*	^{11}C (Corrected)	**19.52 min** *(0.96)*
30 µA		**40 µA**	
^{11}C	17.27 min *(0.85)*	^{11}C	17.63 min *(0.87)*
^{11}C (Corrected)	**19.30 min** *(0.95)*	^{11}C (Corrected)	**19.41 min** *(0.95)*

In Table 3, the values in parentheses are the proportion between the calculated ^{11}C half-lives and the actual half-life. These results demonstrate the effectiveness of amending the data sets to only include the measurements after 20 min. These results also demonstrate that the higher beam currents require additional time post-irradiation for the other contaminant radioisotopes to decay away as more total contaminate radioisotopes are produced at higher beam currents. Overall these results indicate that it would have been beneficial to take measurements for longer than 45 min post-irradiation, particularly at the higher beam currents. However, even with the given results, the corrected data set half-life calculations improve the half-life calculations by 6-10% and indicates that the activity measured between 20-45min is approximately equal to the amount of ^{11}C that is present with minimal contaminant radioisotopes.

The ^{11}C results for each beam current from 20-45 min after the end of irradiation was used to determine the time-zero activity of the ^{11}C. The results from each beam current data set were normalized by µA of beam current and by time of irradiation. The normalized results for 20-45 min were then averaged for each data set. Figure 21 shows these ^{11}C activity per unit charge produced at different beam currents.
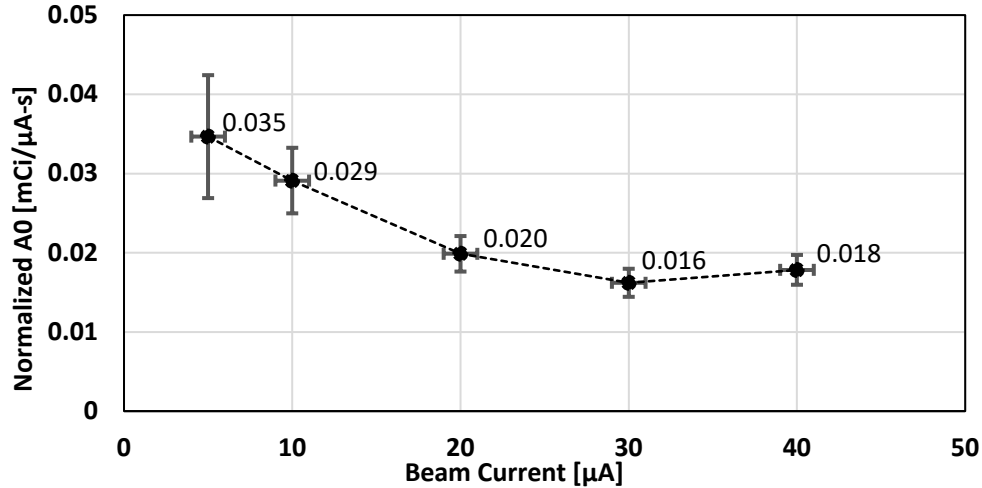
Figure 21: ^{11}C production ion chamber measurements. The results are shown for each beam current data set normalized by μA of beam current and by time (5 min).

It is important to note that the beam current and its uncertainty is accounted for in both the x and y components; however, this representation of the results was the best option for comparing the normalized production with respect to beam current to highlight the effect of gas density reduction. The uncertainty in beam current is approximately ± 1 μA which means that at 5 μA the relative uncertainty is large and decreases as the beam current increases. Additional uncertainty in the normalized activity is primarily from the uncertainty in target irradiation time.

Figure 22 demonstrates that the amount of ^{11}C produced per unit charge decreases as the beam current increases. Although more total ^{11}C is produced at higher beam currents, the production is less efficient. This is likely due to gas density reduction effects. It is also important to note that the loss of efficiency has a large effect at first between approximately 5 to 20 μA and then appears to plateau after that. Between roughly 20 and 40 μA the production efficiency remains approximately the same and differences are within measurement uncertainty.

The ion chamber measurement results were also used to experimentally validate the ^{11}C production simulation. Table 4 shows the normalized experimental results for 5 μA beam current compared to the normalized ^{11}C production simulation results using data from each cross section library.

Table 4: ^{11}C ion chamber experimental results versus production model results.

Cross-Section Data Source	A_0 [mCi/(µA-s)]
Experimental Results (5 µA)	0.035
Simulation (Tabulated Experimental Library)	1.67
Simulation (ENDF)	1.90
Simulation (JENDL)	1.73

One of the factors that is not accounted for in the simulation results is gas density reduction. Based on Figure 21, it appears that gas density reduction effects are occurring and that they can be observed even at beam currents below 10 µA. The cyclotron beam current uncertainty was approximately ±1 µA, so no current below 5 µA was tested for the ion chamber measurements to avoid having uncertainty overwhelm the results. It is possible that gas density reduction effects were occurring at and below 5 µA, and the activity produced per unit charge would be higher at lower beam currents. This could account for some of the discrepancy between the experimental and simulation results.

One factor limiting the exploration of the gas density reduction in the simulation results was uncertainty surrounding the cyclotron target gas region pressure, temperature, and density. During the first set of ^{11}C ion chamber experimental measurements the pressure gauge on the cyclotron target broke. Although the target is known to start at a gas pressure of 165 psi, the temperature and subsequent pressure increases during irradiation were not captured. At the conclusion of this research, the pressure gauge had not yet been replaced, which also prevented the experiment from been replicated to obtain the measurements. Therefore, an accurate representation of the target conditions could not be simulated. To attempt to estimate the conditions, a parameter study was performed by adjusting the density of the target gas in the simulation. The simulation was run with ^{14}N gas densities estimated based on fractional nominal density of 0.013092245 g/cm^3 at a pressure of 165 psi. Table 5 shows a comparison of the results based on density. For these results, a constant average reduced density was assumed throughout the target. This is a non-physical situation since mass must be conserved in the actual target. However, it provides a similar result as a high-fidelity profile. The goal of this parameter study was to represent the density of the part of the target gas region that interacts with the cyclotron

beam. In the actual target, the density of the gas interacting with the beam will decrease and the density of the gas that is not interacting with the beam will increase. The regions of higher density are not interacting with the beam and can be ignored for this simulation.

Table 5: Comparison of A_0 simulated results based on temperature and corresponding density, and pressure of ^{11}C production target gas.

Simulation Cross Section Data Source	$A_0 \left[\frac{mCi}{\mu A-s}\right]$ $\rho = \rho_0$	$A_0 \left[\frac{mCi}{\mu A-s}\right]$ $\rho = 1/2\,\rho_0$	$A_0 \left[\frac{mCi}{\mu A-s}\right]$ $\rho = 1/4\,\rho_0$	$A_0 \left[\frac{mCi}{\mu A-s}\right]$ $\rho = 1/5\,\rho_0$	$A_0 \left[\frac{mCi}{\mu A-s}\right]$ $\rho = 1/10\,\rho_0$
Experimental Data	1.67×10^0	1.22×10^{-1}	7.29×10^{-2}	6.19×10^{-2}	5.26×10^{-2}
ENDF	1.90×10^0	1.43×10^{-1}	8.56×10^{-2}	7.02×10^{-2}	4.99×10^{-2}
JENDL	1.73×10^0	1.26×10^{-1}	7.45×10^{-2}	6.49×10^{-2}	5.54×10^{-2}

As shown in Table 4, the experimental results at 5 µA were 3.5×10^{-2} mCi/(µA-s). The A_0 values at $1/10\,\rho_0$ represent the closest agreement with the experimental results and provide the best representation of the MURR ^{11}C production.

4.4 ^{11}C Production Target Optimization Results

To analyze the production of ^{11}C within the target, a "FMESH" cylindrical mesh control card was added in the gaseous region of the target. The mesh tally measured the flux in each mesh location. The objective of using a mesh tally was to observe beam spreading within the target gas region and determine whether the beam spreads out to the point where it interacts with the target walls. Additionally, the mesh tally allows for the determination of whether the 165 psi nitrogen gas acts as a "thick" target and fully stops the beam within the gas volume.

The results from the mesh tally are shown in Figure 22 and they indicate that the beam does interact with the sides of the target which means that ^{11}C production efficiency is reduced.
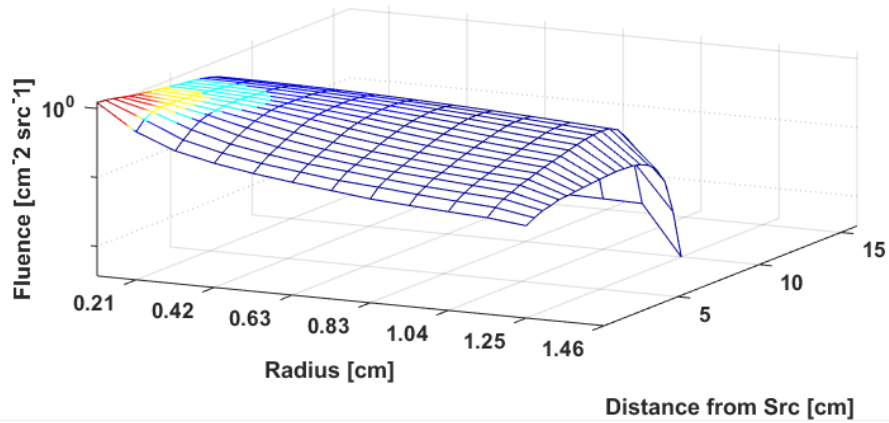
Figure 22: Mesh tally plot for the flux produced in the ^{11}C simulation based on radius and z position in target gas region. Target wall is located at approximately 1.16 cm. The "Distance from Src [cm]" indicates the location along the length of the target with respect to the window where the beam enters.

When the beam begins interacting with the target wall at approximately 1.16 cm, the flux drops off more quickly. This is the expected result since the target walls are solid aluminum. If the target were redesigned in order to accommodate the beam-spreading, then the efficiency of production would be improved. ^{11}C is not produced by proton interaction with Al. Although there is a flux produced in the target walls by proton beam interaction, there is not ^{11}C produced within the walls of the target in the simulation which confirms that that aspect of the code is working as expected.

Table 6 shows the fraction of proton beam energy that interacts with the ^{14}N gas versus the fraction that interacts with the sides of the production target at different gas densities with respect to nominal gas density at 165 psi.

Table 6: The particle flux above the ^{14}N(p,α)^{11}C reaction threshold at varying density relative to nominal density that interacts with the ^{14}N gas versus the amount that interacts with the target walls.

Interaction Region	Flux % $\rho = \rho_0$	Flux % $\rho = 1/2\,\rho_0$	Flux % $\rho = 1/4\,\rho_0$	Flux % $\rho = 1/5\,\rho_0$	Flux % $\rho = 1/10\,\rho_0$
Gas	99.9%	99.24%	90.18%	90.17%	90.16%
Target walls	0.1%	0.76%	9.82%	9.83%	9.84%

48

The values obtained in Table 6 were found by summing the flux values for all of the mesh tally locations. Next, the mesh locations were separated into the locations within the gas region of the target and the locations within the target walls. The flux values for each region were summed and the relative amount of the total in each region is reported. Table 6 demonstrates that although the beam interacts with the target walls, the percentage of the flux that is lost in this way is small compared to the amount that interacts within the gas at higher density. As the density of the target fill gas decreases, the flux fraction that interacts within the target walls increases to roughly 10% at the lowest density values. Based on Table 5, the lowest gas density gives results that are the closest to experimental results. This indicates that the flux efficiency fraction for $1/10 \, \rho_0$ is the most likely and therefore, approximately 10% of the flux is lost to the walls of the target. Another concern associated with the proton beam interacting with the walls is that this can negatively impact the specific activity of the ^{11}C that is produced. Specific activity refers to the relative amount of one isotope to another and is an important quality factor that is used with radioisotopes. The proton beam interacting with the walls of the target can result in other isotopes being produced and detrimentally affect the ^{11}C specific activity. Additional research could be used to explore the impact of redesigning the target to combat this situation.

V. Conclusions

5.1 Summary

This research provides an experimental and computational proof-of-concept for ^{11}C production at MURR. Previous research had demonstrated that stacked foil activation can be used to measure cyclotron beam energy, and radiography could be used to characterize the beam profile. However, these characterization techniques had not been performed for the cyclotron at MURR previously, nor had a model of the production targets been developed. This research improved the ability to model MURR radioisotope production process using MCNP6 to highlight potential areas for target and efficiency improvements in future research.

The proton beam energy was characterized using a stacked foil technique and MCNP6 simulations with ENDF, TENDL, JENDL, and PADF evaluated nuclear data sets. The beam energy was found to be 14.6 ± 0.2 MeV. Additionally, the cyclotron beam was further analyzed through phosphor plate radiography of the cyclotron activated foils. The cyclotron beam profile and intensity were obtained from the radiographic images.

The beam energy, profile, and intensity were then used in the ^{11}C production simulation to model the amount of ^{11}C produced during a MURR production cycle. Ion chamber measurements were obtained and compared to the simulation results in order to experimentally validate the simulation. The ^{11}C production experimental results indicated that the time-zero activity of ^{11}C at a 5 µA beam current is 0.035 mCi/(µA-s). The simulation results for time-zero activity using the constant average density associated with 1/10 nominal density and experimentally determined cross section data was 5.26×10^{-2} mCi/(µA-s), 4.99×10^{-2} mCi/(µA-s) using ENDF cross section data, and 5.54×10^{-2} mCi/(µA-s) using PADF cross section data.

5.2 Simulation Capabilities and Limitations

The ^{11}C production simulation from this project is capable of predicting the amount of ^{11}C that is produced under ideal irradiation conditions. The simulation utilizes an accurate model of the beam energy, profile, and intensity. Additionally, multiple nuclear

cross section data models for the ^{14}N(p,α)^{11}C reaction were incorporated to model the amount of ^{11}C produced.

However, there are several limitations associated with the model that should be stated. During cyclotron irradiation the pressure of the gas in the radioisotope production targets increases due to the heat produced by the beam. The pressure that the target gas reached during irradiation could not be measured due to equipment malfunction, and this factor was not incorporated into the model. Similarly, gas density reduction was not characterized or incorporated. Therefore, the production simulation was limited in its absolute accuracy since the accurate pressure, temperature, and density of the experimental measurements were unknown.

An additional limitation associated with this project was the cyclotron has relatively large uncertainties associated with the irradiation timing and beam current. As a result, the experimental data has a large uncertainty at short irradiation times and low beam currents, which happens to be the ideal conditions to minimize gas density reduction effects. Despite the greater than ideal uncertainty, this research progressed the overall understanding of the MURR cyclotron and radioisotope production.

5.3 Recommendations for Future Research

This project improved the understanding of the MURR cyclotron and radioisotope production. The scope of this research provided an innovative method of integrating experimental and computational methodology to analyze the cyclotron at MURR and the associated production of the radioisotope ^{11}C. The primary achievements of this project are:

- Measurement of the MURR cyclotron proton beam energy
- Characterization of the beam profile and intensity
- Development of a ^{11}C production target simulation
- Analysis of ion chamber measurements to experimentally benchmark the model and explore gas density reduction for ^{11}C production
- Identification of preliminary target design inefficiencies for ^{11}C production

There are additional aspects of the cyclotron and other radioisotope production cycles that could be analyzed which would continue to increase overall understanding of the system. Potential follow-on research includes:

- Conduct additional optimization research of the MURR ^{11}C production target to include specific suggestions for improvement. Adjustments to the target could be simulated to demonstrate increased efficiency in order to make specific suggestions for improvements to the target.

- Incorporate the gas density reduction effects in the ^{11}C production simulation that were determined to be present during radioisotope production with this target.

- Phosphor imaging with sufficient resolution to capture the natural angular divergence of the cyclotron beam.

- Extend this research to the MURR cyclotron deuteron beam: Measure the precise energy of the MURR cyclotron deuteron beam. Similar methodology could be used but it would require a separate analysis of the ideal stacked foil material and arrangement that could be used. Conduct phosphor plate radiographic imaging of the deuteron beam irradiated foils could be used to analyze the beam shape and intensity. Simulate MURR ^{13}N production via the ^{12}C(d,n)^{13}N reaction. This would include modeling the production target and experimentally validating the model. Perform an optimization analysis of the MURR ^{13}N production target using the ^{13}N production model.

Appendix A. MURR HPGe Specifications

Eckert & Ziegler
Analytics

1380 Seaboard Industrial Blvd.
Atlanta, Georgia 30318
Tel 404·352·8677
Fax 404·352·2837
www.ezag.com

CERTIFICATE OF CALIBRATION
Standard Reference Source

HP#: 21-17-04

SRS Number: 106492
Source Description: Point Source in Aluminum Card
Product Code: 8401-GF-PNT-CUS
Customer: University of Missouri
P.O. Number: HULEN28APR17/MC, Item 1

This standard radionuclide source was prepared from an aliquot measured gravimetrically from a master radionuclide solution calibrated with a germanium gamma-ray spectrometer system. Additional radionuclides were added gravimetrically from solutions calibrated by gamma-ray spectrometry, ionization chamber, or liquid scintillation counting. Calibration and purity were checked using germanium gamma-ray spectrometry. At the time of calibration no interfering gamma-ray emitting impurities were detected. The gamma-ray emission rates for the most intense gamma-ray lines are given. Eckert & Ziegler Analytics (EZA) maintains traceability to the National Institute of Standards and Technology (NIST) through a Measurements Assurance Program as described in USNRC Regulatory Guide 4.15, Revision 2, July 2007, and compliance with ANSI N42.22-1995, "Traceability of Radioactive Sources to NIST."

Reference Date: 01-July-2017   12:00 PM EST

MGS Mixture

Isotope	Gamma-Ray Energy, keV	Half-Life, d	Activity, Bq	Flux, s⁻¹	u_A, %	u_B, %	U, %*	Calibration Method**
Am-241	59.5	1.580E+05	2.212E+04	7.940E+03	0.1	1.8	3.6	4π LS
Cd-109	88.0	4.614E+02	3.100E+05	1.147E+04	0.5	2.0	4.1	HPGe
Co-57	122.1	2.717E+02	7.146E+03	6.117E+03	0.4	1.7	3.4	HPGe
Ce-139	165.9	1.376E+02	1.065E+04	8.523E+03	0.4	1.7	3.6	HPGe
Hg-203	279.2	4.659E+01	2.254E+04	1.838E+04	0.3	1.7	3.5	HPGe
Sn-113	391.7	1.151E+02	1.844E+04	1.198E+04	0.4	1.9	3.9	HPGe
Cs-137	661.7	1.099E+04	8.849E+03	7.530E+03	0.7	1.9	4.1	HPGe
Y-88	898.0	1.066E+02	3.070E+04	2.876E+04	0.7	1.7	3.7	HPGe
Y-88	1836.1	————	————	3.045E+04	0.7	1.7	3.7	————
Co-60	1173.2	1.925E+03	1.459E+04	1.457E+04	0.7	1.8	3.9	HPGe
Co-60	1332.5	————	————	1.459E+04	0.7	1.8	3.9	————

Mixed Gamma (MGS) master solution is EZA's eight isotope mixture which is calibrated quarterly and consists of Cd-109, Co-57, Ce-139, Hg-203, Sn-113, Cs-137, Y-88, and Co-60. **Uncertainty:** U - Relative expanded uncertainty, k = 2. See NIST Technical Note 1297, "Guidelines for Evaluating and Expressing the Uncertainty of NIST Measurement Results." **Calibration Methods:** 4π LS - 4π Liquid Scintillation Counting, HPGe - High Purity Germanium Gamma-Ray Spectrometer, IC - Ionization Chamber.

(Certificate continued on reverse side)

F-CR-32, Rev. 0, 01 Nov 14

Corporate Office
24937 Avenue Tibbitts   Valencia, California 91355

Laboratory
1380 Seaboard Industrial Blvd. Atlanta, Georgia, 30318

QUALITY ASSURANCE DATA SHEET
GMX SERIES GAMMA-X HPGE
(HIGH-PURITY GERMANIUM) COAXIAL PHOTON DETECTOR SYSTEM

MODEL AND SERIAL NUMBERS

Detector Model No. _GMX-25190-P_

Cryostat Configuration _PopTop_

Dewar Model _—_

Preamplifier Model _237N_

Preamplifier S/N _747_

H.V. Filter Model _138_

H.V. Filter S/N _6085_

Smart-1-N _—_

IMPORTANT REFERENCE DATA

Ship Date _8-12-10_

Serial No. _31-TN10688A_

When calling Customer Service, always reference this Detector Serial No.

Dewar Capacity _—_   Static Holding Time _—_   Detector Cool-Down Time _—_

DIMENSIONS

Detector Diameter _54.5_ mm

Detector Length _48.4_ mm

End Cap to Detector _3_ mm

ABSORBING LAYERS

Beryllium _0.50_ mm

Aluminum _—_ mm

Inactive Germanium – 0.3 μm

Recommended Operating Bias, NEGATIVE _2500_ V

PERFORMANCE SPECIFICATIONS*

|	Warranted	Measured	Amplifier Time Constant
Resolution (FWHM) at 1.33 MeV, ^{60}Co	2.09 keV	1.85 keV	6 μs
Peak-to-Compton Ratio, ^{60}Co	43:1	52:1	6 μs
Relative Efficiency at 1.33 MeV, ^{60}Co	22.5 %	25.0 %	6 μs
Peak Shape (FWTM/FWHM), ^{60}Co	1.95	1.87	6 μs
Peak Shape (FWFM/FWHM), ^{60}Co		2.57	6 μs
Resolution (FWHM) at 5.9 keV, ^{55}Fe	759 eV	567 eV	6 μs

*Measured at a nominal rate of 1000 counts/s unless otherwise specified.
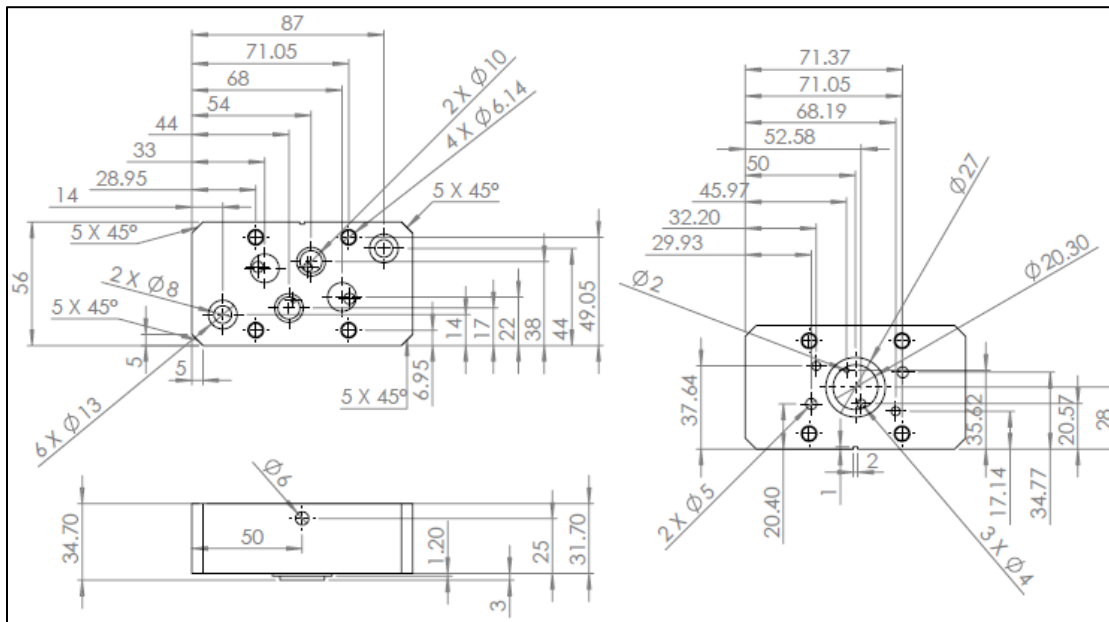
Other: _Capsule SCA # 2098_
cryostat PV-1 # 2208

Data Certified by: _BS Wilson_   Date: _8-11-10_

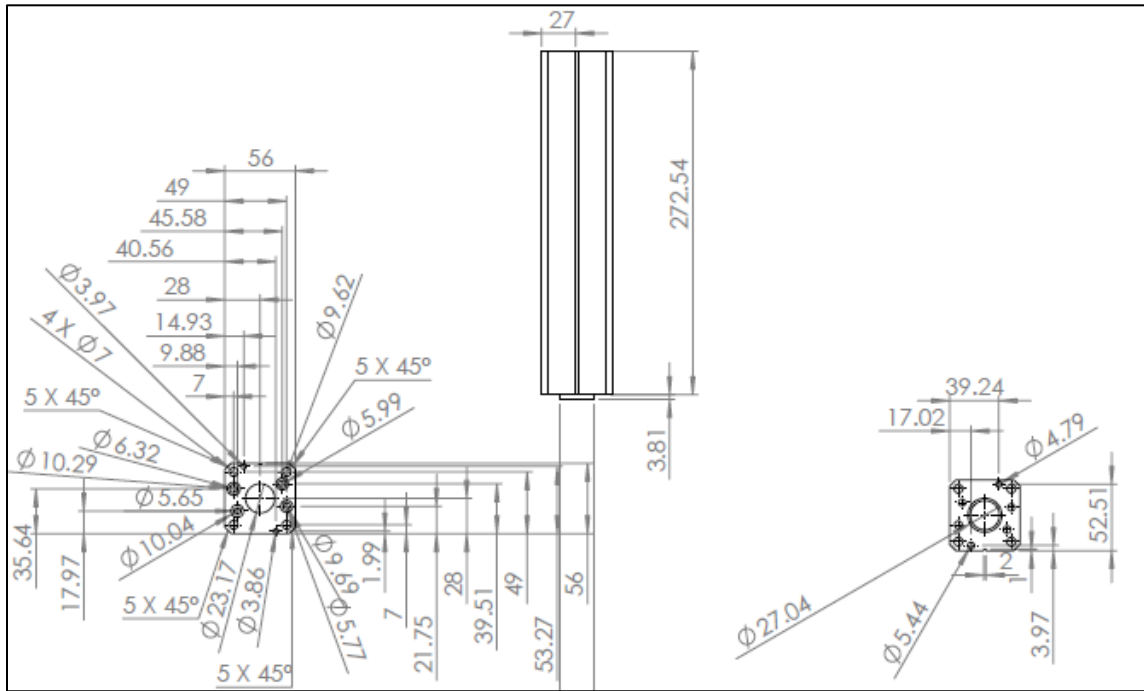# Appendix B. ^{11}C Production Target Schematics

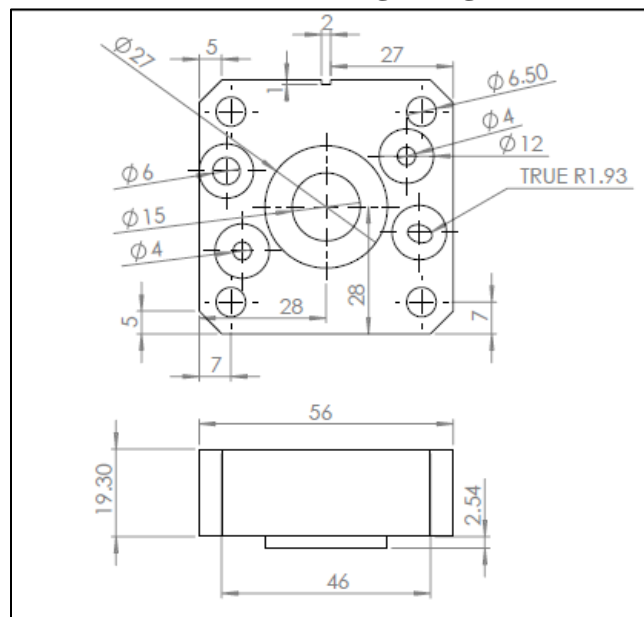## Full Target Diagram with Specification Chart
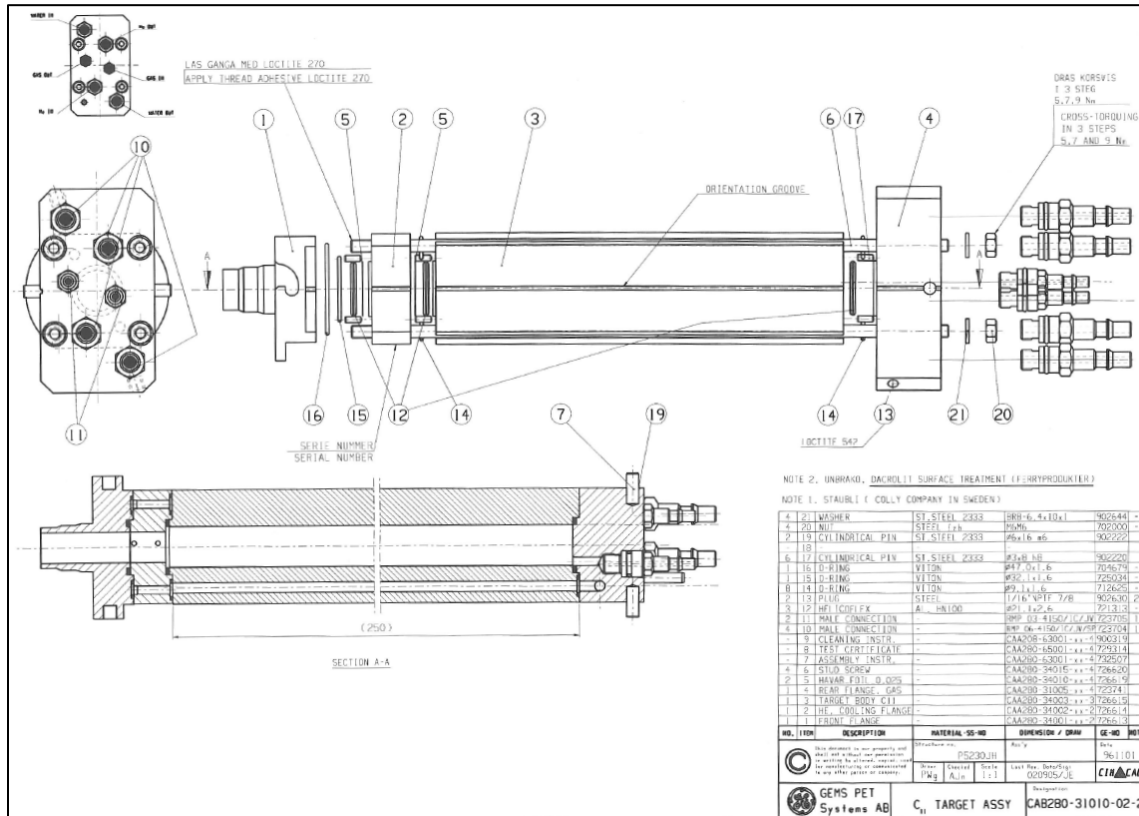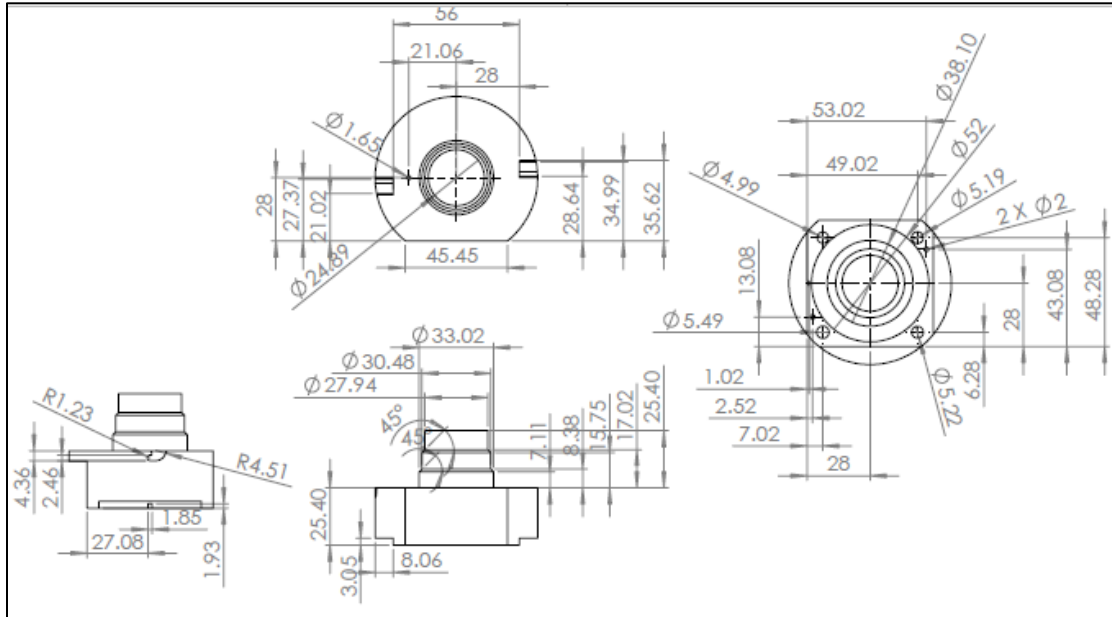

Rear Gas Flange

¹¹C Target Body

Helium Cooling Flange

56

Front Flange

Appendix C.   GitHub Repository

The simulation input files and Python codes for this research described above are provided in a private online repository on GitHub at the following location: *https://github.com/Bevins-Research-Group/N13_Project/Research_Models*. For access to this repository, please contact the author.

The **Research Models** directory contains the following sub-directories:

- **Activation Foils**: This subdirectory contains the stacked foil activation simulation and a solid angle calculator for foils.

- **^{11}C Production Model**: This subdirectory contains the final ^{11}C production simulation for this research and the previous version which contains the original proton beam characterization.

- **Mesh Tally Analysis**: This subdirectory contains the final ^{11}C production simulation including the mesh tally and two MATLAB codes that read the outputs of the mesh tally.

- **Additional Files**: This subdirectory contains TENDL cross section information for isotopes included in the ^{11}C production simulations.

Bibliography

[1] American Nuclear Society Medical Use of Radioisotopes Center for Nuclear Science and Technology Information, 2014.

[2] Gómez, Sara, et al. "Methyl Jasmonate Elicits Rapid Changes in Carbon and Nitrogen Dynamics in Tomato." New Phytologist, vol. 188, no. 3, 2010, pp. 835–844., doi:10.1111/j.1469-8137.2010.03414.x.

[3] Dewey, Sl, et al. "GABAergic Inhibition of Endogenous Dopamine Release Measured in Vivo with 11C-Raclopride and Positron Emission Tomography." The Journal of Neuroscience, vol. 12, no. 10, 1992, pp. 3773–3780., doi:10.1523/jneurosci.12-10-03773.1992.

[4] Jeffries, Bradley Characterization of Fast Neutron Irradiation Positions at a 16.5 MeV PET-Trace Cyclotron Missouri University Research Reactor, 1513 Research Park Drive, Columbia, Missouri 65211.

[5] "Richard Ferrieri Biography." Richard Ferrieri – University of Missouri (MURR) Chemistry, 2018, https://chemistry.missouri.edu/people/ferrieri

[6] Jeffrey E. Williams. Donner Laboratory: The Birthplace of Nuclear Medicine. Journal of Nuclear Medicine, 1 January 1999, jnm.snmjournals.org/content/40/1/16N.citation.

[7] Health Effects of Project SHAD Chemical Agent: Phosphorous-32. The Center for Research Information, Inc., 2004, Health Effects of Project SHAD Chemical Agent: Phosphorous-32, www.nationalacademies.org/hmd/~/media/Files/Report%20Files/2007/Long-Term-Health-Effects-of-Participation-in-Project-SHAD-Shipboard-Hazard-and-Defense/PHOSPHORUS32.pdf.

[8] Tollefson, Jeff. Reactor Shutdown Threatens World's Medical-Isotope Supply. Nature News, Nature Publishing Group, 12 September 2016, www.nature.com/news/reactor-shutdown-threatens-world-s-medical-isotope-supply-1.20577.

[9] Pankievicz, Vânia C. S., et al. "Robust Biological Nitrogen Fixation in a Model Grass-Bacterial Association." The Plant Journal, vol. 81, no. 6, 2015, pp. 907–919., doi:10.1111/tpj.12777.

[10] Los Alamos National Laboratory, "LA-CP-13-00634: MCNP6 User's Manual," May 2013.

[11] TALYS-Based Evaluated Nuclear Data Library. TENDL-2015 Nuclear Data Library https://tendl.web.psi.ch/tendl2015/tendl2015.html

[12] "JENDL-4.0." Nuclear Data Center - Japan Atomic Energy Center, 2014, wwwndc.jaea.go.jp/jendl/j40/j40.html.

[13] "The Proton Activation Data File PADF-2007 in ENDF-6 Format." IAEA Nuclear Data Services, 2007, www-nds.iaea.org/padf/.

[14] "Evaluated Nuclear Data File (ENDF)." IAEA Nuclear Data Services, www-nds.iaea.org/exfor/endf.htm.

[15] "JANIS." Executive Summary -Chernobyl: Assessment of Radiological and Health Impact, Nuclear Energy Agency (NEA), www.oecd-nea.org/janisweb/.

[16] Kopecký, Petr. "Proton Beam Monitoring via the Cu(p, x)58Co, 63Cu(p, 2n)62Zn and 65Cu(p, n) 65Zn Reactions in Copper." The International Journal of Applied Radiation and Isotopes, vol. 36, no. 8, 1985, pp. 657–661., doi:10.1016/0020-708x(85)90008-0.

[17] Burrage, J. W., et al. "A Simple Method to Measure Proton Beam Energy in a Standard Medical Cyclotron." Australasian Physics & Engineering Sciences in Medicine, vol. 32, no. 2, 2009, pp. 92–97., doi:10.1007/bf03178634.

[18] Khandaker, Mayeen Uddin, et al. "1. Investigations of Proton Beam Energy of the MC-50 Cyclotron at KIRAMS." International Journal of Physical Sciences, vol. 6, no. 13, 31 July 2011, pp. 3168–317., doi:76248E821725.

[19] "Cyclotron Produced Radionuclides: Operation and Maintenance of Gas and Liquid Targets." IAEA Radioisotopes and Radiopharmaceuticals Series Publications, Ch. 5, International Atomic Energy Agency, 2012, www-pub.iaea.org/MTCD/Publications/PDF/Pub1563_web.pdf.

[20] Ferrieri, Richard A., et al. "Use of Carbon-11 in Populus Shows That Exogenous Jasmonic Acid Increases Biosynthesis of Isoprene from Recently Fixed Carbon." Plant, Cell and Environment, vol. 28, no. 5, 2005, pp. 591–602., doi:10.1111/j.1365-3040.2004.01303.x.

[21] Krane, Kenneth S. *Introductory Nuclear Physics*. Wiley, 1988.

[22] Takács, S., et al. "Validation and Upgrading of the Recommended Cross Section Data of Charged Particle Monitor Reactions." Nd2007, 2007, doi:10.1051/ndata:07349.

[23] Ingalls, P. D., et al. "14N(p,Alpha) Cross Sections from 3.8 to 6.4 MeV." Physical Review, vol. 13, Feb. 1976. Nuclear Physics, doi:J,PR/C,13,524,197602.20

[24] Canberra Industries, Inc. Genie™ 2000 Spectroscopy Software Operations. Genie™ 2000 Spectroscopy Software Operations, 2006.

[25] General Electric (GE) Company. Phosphor Imaging Plates - Computed Radiography. Phosphor Imaging Plates - Computed Radiography, 2010.

[26] Radiation Detection and Measurement, by Glenn F. Knoll, 4th ed., John Wiley & Sons, Inc., 2010, pp. 131–158.

[27] "Scipy.stats.ks_2samp." Scipy.stats.trim_mean - SciPy v1.1.0 Reference Guide, Scipy.org, docs.scipy.org/doc/scipy/reference/generated/scipy.stats.ks_2samp.html.

[28] "Scipy.stats.chisquare." SciPy v1.1.0 Reference Guide, docs.scipy.org/doc/scipy/reference/generated/scipy.stats.chisquare.html.

[29] General Electric (GE). "PETtrace 800 Cyclotron Series Data Sheet." GE Healthcare, www3.gehealthcare.com/~/media/downloads/us/product/product-categories/moleculer%20imaging/pet%20radiopharmacy/cyclotrons/pt800%20cyclotron%20system%20data%20sheet%20rev3.pdf?Parent=%7B442067E1-C933-4B8E-8D5B-1DBC294ECE21%7D.

[30] "Relationship between Density, Pressure, and Temperature." Chapter 1. Stony Brook University. http://msrc.sunysb.edu/~chang/atm205/Notes/Chapter_1_txtb.pdf.

[31] Nam, S.k., and K.b. Kim. "Transverse Profile Measurement of Proton Beam Using the Beam Induced Fluorescence Monitor in KIRAMS-13 Cyclotron." Journal of the Korean Vacuum Society, vol. 18, no. 6, 2009, pp. 418–425., doi:10.5757/jkvs.2009.18.6.418.

[32] "Hypothesis Testing and Model-Fitting." Swinburne Astronomy Online. http://astronomy.swin.edu.au/~cblake/StatsLecture3.pdf.

[33] Schlyer, David J. "Heat Transfer in Cyclotron Targets." Brookhaven Science Associates U.S. Department of Energy.

[34] Q-Value Calculator (QCalc), www.nndc.bnl.gov/qcalc/.